A Clearer Picture of Musculoskeletal Disorders of the Knee and Thumb Through the Lens of Image-Based Finite Element Analysis

By
Nolan M. Norton
M.S. Bioengineering, University of Kansas, 2018
B.S. Chemical Engineering, University of Alabama, 2016

Submitted to the graduate degree program in Bioengineering and the Graduate Faculty of the University of Kansas School of Engineering in partial fulfillment of the requirements for the degree of Doctor of Philosophy.

Chair: Kenneth J. Fischer, Ph.D.

Suzanne M. Shontz, Ph.D.

Anil Misra, Ph.D., P.E., F.ASCE

Sara E. Wilson, Ph.D.

Terence E McIff, Ph.D.

Date Defended: 12/3/2021

The dissertation committee for Nolan M. Norton certifies that this is the approved version of the following dissertation:

A Clearer Picture of Musculoskeletal Disorders of the Knee and Thumb Through the Lens of Image-Based Finite Element Analysis

Chair: Kenneth J. Fischer, Ph.D.

Suzanne M. Shontz, Ph.D.

Anil Misra, Ph.D., P.E., F.ASCE

Sara E. Wilson, Ph.D.

Terence E McIff, Ph.D.

Date Approved: 12/10/2021

Abstract

The first goal of this work was to understand the contributions of intra-cyst fluid pressure to the growth of subchondral bone cysts (SBCs). The equine stifle joint provides a natural animal model for studying SBCs. Finite element models were used to examine three cyst sizes of approximately 0.03 cm^3 (C1), 0.5 cm^3 (C2), and 1 cm^3 (C3) in the equine stifle joint. Fluid pressure was simulated by using a soft solid filling or empty-cysts with uniform pressure loads. The models suggest that shear stresses due to joint loading, not pressurized fluid, are likely the cause of damage to the subchondral bone.

The second goal of this work was to develop a modular MRI-compatible micropipette simulator that could be used for MRI-based FEA of the basilar thumb joint. A modular MRI-compatible micropipette simulator addresses several limitations of pipetting studies, and it can be used to isolate micropipette design features to understand how they affect basilar thumb joint contact mechanics. A micropipette simulator with a cylindrical handle (length 127 mm, diameter 25 mm) was used with one subject to demonstrate the system's feasibility. Contact area, pressure, and location were similar to previously published data of basilar thumb joint models in power grasp and lateral pinch. The simulator's modularity will allow future studies to examine handle design parameters such as handle diameter, cross-sectional shape, and other features.

The third goal of this work was to utilize the modular MRI-compatible micropipette simulator to analyze the effects of three handle diameters (12 mm, 25 mm, and 40 mm) and finger rest inclusion on basilar thumb joint contact mechanics. All contact measures decreased with increasing handle diameter. Contact area and force were higher with a finger rest. We expected contact measures to decrease with the presence of a finger rest. The unexpected outcome may have been due to non-randomized test order and fatigue during testing.

Acknowledgements

"Well, here at last, dear friends, on the shores of the Sea comes the end of our fellowship in Middle-earth. Go in peace! I will not say: do not weep; for not all tears are an evil." – Gandalf, The Return of the King: The Grey Havens

It is difficult to pick where to begin my appreciation. This is the end of a journey that could not have been accomplished alone. First, I thank my advisor Dr. Kenneth Fischer. These past few years have been filled with numerous challenges beyond those of research and academics. He has been supportive and understanding through everything while also providing professional guidance and mentorship. I thank my committee members, specifically Dr. Sara Wilson, whom I had the pleasure of assisting in the classroom for several semesters, Dr. Suzanne Shontz, Dr. Anil Misra, and Dr. Terence McIff whose lab I've had the pleasure to know and work with throughout these past few years. I thank Lance Frazer for recruiting me to the Musculoskeletal Biomechanics Lab. His help and support were critical in helping me to succeed; his efforts and friendship are greatly appreciated. Numerous other friends have helped me along the way. Namely, Denise, Carsten, Kyle, Aparna, Ankit, Joe, Settimio, Aishik, Grahmm, and many others. Lastly, I would not be here without the support of my family. Unfortunately, Mom passed away in January 2019 due to cancer and could not physically see me finish my degree. However, she still lives on in my life and in those whose lives she touched. Even when treatments and outcomes did not go her way, she was a true example of kindness, positivity, and determination that I can draw upon in difficult moments. I know that she and her dad, J. P. Shugars who received his PhD in Horticulture from the University of Tennessee in 1970 and passed away in 2011, are especially proud. Thank you Dad, Wes, Diane, Luke, and Miles. All of you have provided a great amount of support and encouragement on this journey.

Table of Contents

Table of Figures

1. Extended Summary

Osteoarthritis (OA) is considered to be a multifactorial disease of the entire joint. Mechanical loads are one of the contributing factors to the development of OA in the knee and hand. Other musculoskeletal disease conditions in the knee, such as subchondral bone cysts (SBCs), are also affected by mechanical loads. Imaging and other experimental methodologies have been used to study OA. These types of studies can provide useful data, but they are limited in several ways such as difficulties capturing images during joint loading, image quality, their invasive nature, and a dissimilarity between experimental and in vivo environments. Computational methodologies, such as finite element analysis (FEA), can be used to address some imaging and experimental limitations. In this work, FEA was used to analyze mechanical contributions to musculoskeletal diseases in the equine stifle joint, an animal model of the human knee, and the basilar thumb joint.

The first goal of this work was to understand the contributions of intra-cyst fluid pressure to the growth of SBCs. The etiology of SBCs is not fully understood. Mechanical trauma due to repeated or large loads and trauma due to fluid pressure are two mechanisms believed to cause their formation and growth. The equine stifle joint provides a natural animal model for studying SBCs. FEAs of the equine stifle joint were used to examine three cyst sizes of approximately 0.03 cm^3 (C1), 0.5 cm^3 (C2), and 1 cm^3 (C3). Two types of simulations, cysts with a soft solid filling and empty-cysts with uniform pressure loads, were used to simulate fluid pressurization. The models suggest that shear stresses due to joint loading are likely the cause of damage to the subchondral bone and not pressurized fluid from the joint.

The second goal of this work was to develop and demonstrate a modular MRI-compatible micropipette simulator that could be used for MRI-based FEA of the basilar thumb joint. The

basilar thumb joint is commonly affected by OA. Many laboratory technicians and researchers who frequently use pipettes experience hand and upper limb disorders. A modular MRI-compatible micropipette simulator can be used to isolate micropipette design features to understand how they affect basilar thumb joint contact mechanics. A micropipette simulator with a cylindrical handle (length = 127 mm, diameter = 25 mm) was used with one subject to demonstrate the system's feasibility. Contact area, pressure, and location were similar to previously published data of basilar thumb joint models in power grasp and lateral pinch. The micropipette simulator addresses several limitations of current techniques for studying pipetting and provides an ability to gain insight into basilar thumb joint mechanics. It's modularity will allow future studies to examine handle design parameters such as handle diameter, cross-sectional shape, and other features.

The third goal of this work was to utilize the modular MRI-compatible micropipette simulator to analyze the effects of handle diameter and finger rest inclusion on basilar thumb joint contact mechanics. This study examined the effect of three micropipette handle diameters (12 mm, 25 mm, and 40 mm) and the presence of a finger rest on contact area, contact force, and peak contact pressure in the basilar thumb joint. All contact measures decreased with increasing handle diameter. There were significant differences for all contact measures between the 12 mm diameter and the 40 mm diameter handles. Decreasing contact measures with increasing diameter confirmed our hypothesis for the handle diameter examination. Contact area and force were higher with a finger rest. We expected contact measures to decrease with the presence of a finger rest. The unexpected outcome may have been due to non-randomized test order and fatigue during testing.

This work demonstrates the use of FEA to understand mechanical contributions to

musculoskeletal disease in commonly affected joints. The equine stifle joint has been used to understand contributing factors to SBC growth without the presence of confounding effects due to OA. Future efforts could focus on human models of SBCs, which will more likely be affected by OA presence, to gain further clarity on the state of subchondral bone and its role throughout SBC development. The modular micropipette simulator is also compatible with other imaging modalities, so it could be used with other types of imaging and experimental studies. The micropipette simulator's modularity allows for different handle designs to be easily implemented. Design variations that focus on handle texture, hardness, weight, and cross-sectional shape are a few options for future studies.

2. Introduction

2.1 Osteoarthritis Definition, Effects, and Treatments

2.1.1 Definition, Trends, and Commonly Affected Joints

Musculoskeletal disorders are some of the most common ailments in the United States and globally. Osteoarthritis (OA) is one of the most common musculoskeletal disorders and the most common form of arthritis. Historically, OA has been characterized by progressive degenerative changes to articular cartilage in one or more joints. Current research indicates that the disease is more complicated than previously thought. Approximates of OA prevalence are 31 million people in the United States and 300 million people globally [1, 2]. It is the leading cause of pain and disability in older adults with an estimated cost of $303 billion in medical expenses and lost wages in 2013 [3]. The knee and the hand are among the areas most commonly affected by OA. Prevalence rates for symptomatic OA, defined as a person with OA who experiences some of its known symptoms, in the hand have been reported from 8.2%-13.3% for men and 15.9%-26.2% for women [4, 5]. Prevalence rates for symptomatic OA in the knee have been

reported from 6.8%-13.5% for men and 11.4%-18.7% for women [6, 7]. The incidence of OA increased from 1997-2017, and that trend is expected to continue due to increased life expectancy and population growth [8].

2.1.2 Factors Affecting OA and Its Lasting Effects

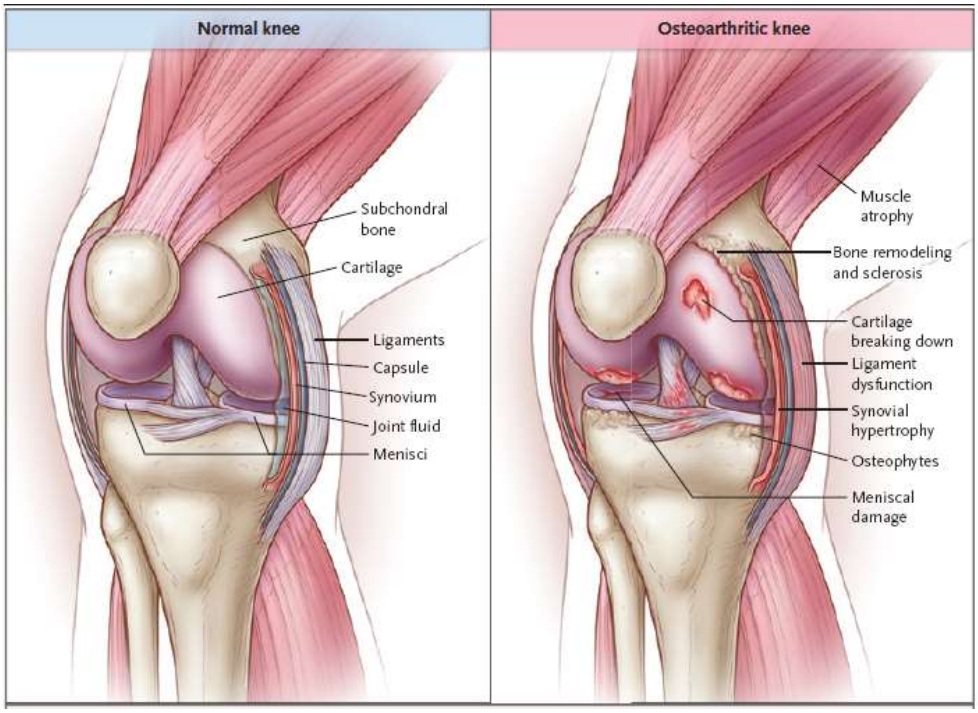

Figure 2.1. Differences between a normal and osteoarthritic knee. Reproduced with permission from Sharma, L, *Osteoarthritis of the Knee*. N Engl J Med, 2021. 384: p. 51-59, Copyright Massachusetts Medical Society.

OA was once thought to be a product of wear and tear on the joint due to repeated mechanical loads, but recent research has led to the understanding that it is a condition of the entire joint that is influenced by several factors. OA characterization now includes changes in articular cartilage, changes in the subchondral bone, and synovitis (Figure 2.1). The exact pathophysiology of OA is still unclear, but it is believed that complex interactions between mechanical, biochemical, and cellular factors contribute to OA initiation and progression. The factor that poses the greatest risk to OA development is age. A higher prevalence of OA has been

reported in older age groups [6, 7, 9, 10]. This could be due to a myriad of reasons. Changes in hormonal levels, muscular strength, slower reflexes, and tissue stability and structure could contribute to conditions conducive to OA development. A second factor that affects OA development is sex. In particular, women aged 60 or older have generally reported OA more commonly than men in the same age group [9, 10]. Differences in hormones, bone morphology, and joint congruence have been proposed as contributors to this observed trend. Some studies have reported higher prevalence rates in men under 60 years old [9, 10] whereas some studies have reported higher prevalence rates in women in all age groups [6, 7]. A third factor that influences OA development is the nature and duration of mechanical loading. Chondrocytes within articular cartilage are highly sensitized to mechanical loads and produce biochemical signals in response to them that drive bone remodeling. Weight-bearing exercise has been shown to increase bone mineral density [11] and an increase in biomarkers which indicate bone remodeling [12]. However, abnormal loads, either through magnitude, duration, frequency, or location, produce detrimental changes that lead to joint degradation. Previous injuries to a joint can affect how joints distribute mechanical loads. Traumatic injuries can affect surrounding soft tissues and musculature in addition to bone. Changes in surrounding tissue can impact their ability to stabilize a particular joint, and changes in bone morphology due to injury can impact contact mechanics by shifting, increasing, or decreasing contact. These changes can contribute to the development of OA. Other risk factors include obesity, genetics, ethnicity, and occupation. Chronic effects of OA in the hand and knee include pain, cramping, joint swelling, joint locking, and joint instability. These create long-term difficulties such as loss of mobility, loss of function, and long recovery times after which function may not be fully restored. Secondary effects include increased healthcare costs, lost wages, and decreased productivity.

2.1.3 OA Diagnosis and Treatments

A combination of physical examinations and imaging techniques are used to test for the presence of OA and assess its severity. Physical examinations are utilized before imaging techniques. Physical examinations of the knee include checking for crepitus, flexion contracture, tenderness, swelling, mild warmth, and bony enlargements. Additionally, an assessment of standing alignment or gait can reveal any instability or misalignments. Physical examinations are sometimes sufficient to assess if OA is present and determine its severity. However, additional imaging measures may be utilized to gather more data before a diagnosis. Radiography is the most common imaging modality used to assess OA in both the knee and hand. Radiographic OA is defined as joints that meet specific visual criteria for OA on radiographic images. Radiography provides a non-invasive view of joints, but it can't detect early articular or soft tissue damage. Other imaging modalities, such as ultrasound and magnetic resonance imaging (MRI), can provide details about the condition of articular cartilage and other soft tissues, but they are not commonly used in clinical practice. The Kellgren-Lawrence system is widely used to assess radiographic knee OA (Table 2.1).

Table 2.1. Kellgren-Lawrence Radiographic Grading System [13]	
Grade (OA Severity)	Description
0 (none)	No joint space narrowing or changes due to OA
1 (doubtful)	Doubtful joint space narrowing, possible osteophytic lipping
2 (minimal)	Possible joint space narrowing, definite osteophytes
3 (moderate)	Definite joint space narrowing, moderate osteophytes, some sclerosis, possible deformity of the bone ends
4 (severe)	Marked joint space narrowing, large osteophytes, severe sclerosis, definite deformity of the bone ends

Common imaging practices for the knee include a posteroanterior (PA) radiographic view while standing or bearing weight and a lateral or skyline view of the patellofemoral compartment. These images allow for the assessment of subchondral sclerosis, bone cysts, osteophytes, and asymmetrical joint space narrowing (Figure 2.2).

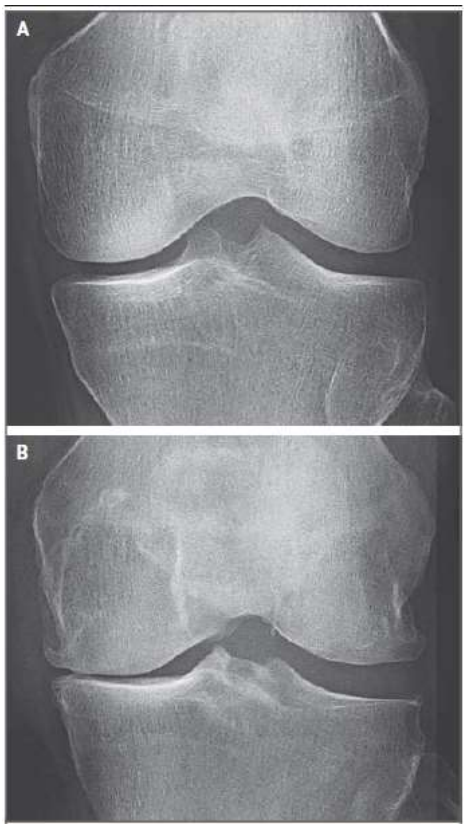

Figure 2.2. Radiographic image of a knee for assessment of osteoarthritis. (A) A radiographic image of a normal knee. (B) A radiographic image of an osteoarthritic knee with joint space narrowing, subchondral sclerosis, and marginal osteophytes. Reproduced with permission from Sharma, L, *Osteoarthritis of the Knee*. N Engl J Med, 2021. 384: p. 51-59, Copyright Massachusetts Medical Society.

The basilar thumb joint is the second most affected joint in the hand behind the distal interphalangeal joints [10, 14]. Physical examinations of the basilar thumb joint include checking for localized pain using the grind test or the traction-shift test, swelling, crepitus, instability, and decreased grip strength using either key pinch or power grasp. Stiffness and adduction of the basilar joint are also indications of advanced disease. The Eaton-Littler system, which was later

updated by Eaton and Glickel, is the most commonly used to assess OA severity in the basilar thumb joint (Table 2.2).

Table 2.2. Eaton-Littler [15] and Eaton-Glickel [16] Classification Systems		
Grade	Eaton-Littler Description	Eaton-Glickel Description
1	Normal articular contours, slight widening of the joint space, less than 1/3 subluxation in any direction	Normal articular contours, slight widening of the joint space
2	At least 1/3 subluxation of the joint, osteophytes or loose bodies smaller than 2 mm	Slight narrowing of joint space, minimal sclerotic changes of subchondral bone, osteophytes or loose bodies smaller than 2 mm
3	Slight joint space narrowing, greater than 1/3 subluxation is present, osteophytes and loose bodies greater than 2 mm	Markedly narrowed joint space, many cystic changes and sclerotic bone, osteophytes and loose bodies greater than 2 mm, some dorsal subluxation
4	Markedly narrow joint space, sclerotic and cystic changes present, major subluxation present, margins of trapezium show lipping and osteophyte formation	Complete deterioration of joint, scapho-trapezial joint narrowed with sclerotic and cystic changes

Common imaging practices for the basilar thumb joint include PA, lateral, and oblique radiographic views of the hand and wrist. Imaging views focused on the basilar thumb joint include the Roberts view, a true anteroposterior view of the joint, and the Betts view, a true lateral of the joint (Figure 2.3). Additionally, a stress radiograph from the PA view of the hand may be used to assess basilar thumb joint subluxation and stability [17]. The severity of OA, as determined by a combination of physical examinations, imaging, and patient comfort levels are used to determine the course of treatment.

Figure 2.3. Common radiographic imaging views of the basilar thumb joint. (A) A Robert's view of basilar thumb joint. (B) A lateral view of the basilar thumb joint. (C) A Bett's view of the basilar thumb joint. Reproduced with permission from Spaans, AJ et al., *Interobserver Agreement of the Eaton-Littler Classification System and Treatment Strategy of Thumb Carpometacarpal Joint Osteoarthritis*. The Journal of Hand Surgery (American Ed.), 2011. 36: p. 1467-1470).

Early treatments of OA focus on managing joint stiffness and pain with conservative techniques. These include exercise routines to help strengthen muscles around a joint and increase stability and promote weight loss. Other conservative treatment techniques are the use

of braces or crutches, dietary changes, and nonsteroidal anti-inflammatory drugs taken either orally or through intraarticular injections. Surgical interventions are a possibility, but they are only used when patients continue to experience significant pain and do not respond to conservative treatment plans. Total joint arthroplasty is the gold standard of surgical treatment of the knee. However, joint replacement failures can be difficult and costly to replace so care is taken to exhaust other options until it is deemed necessary. Other surgical options for the knee include arthroscopic debridement and lavage, osteotomy, and unicompartmental arthroplasty. There are several surgical options for treating basilar thumb joint OA. These include arthroscopic debridement for early stage OA, extension osteotomy, partial or complete trapeziectomy, trapeziectomy with ligament reconstruction and tendon interposition, arthrodesis, and implant arthroplasty. Surgical procedures are determined by the patient's condition, either early or advanced OA, and the surgeon's experience with different techniques. Comprehensive studies are still needed to adequately compare patient outcomes from different basilar joint surgical techniques.

Despite the frequency of OA occurrence and its impact, there is no cure and much to learn about it. The evolving understanding of OA's complexity has several effects on its research. It has introduced complex questions about its etiology and how different factors and conditions contribute to its progression within different joints. The complexities of OA cannot be fully understood through one perspective. Imaging, in vitro and in vivo, and computational studies are example classifications of methodologies that are used to research OA. Each of these provide different lenses that offer unique insights into OA initiation and progression.

2.2 Methods Used to Study OA

2.2.1 Imaging Studies

Several imaging modalities have been used to study OA. The most common is radiography. Radiography provides a two-dimensional image of dense tissue such as bone. Radiographic images can provide both semi-quantitative and completely quantitative measures that assess the severity and progression of OA. Grading systems, such as the Kellgren-Lawrence system, are used to provide semi-quantitative assessments of joint space narrowing, presence of osteophytes and their size, sclerosis, and the presence of cysts. Joint space width, for example, can be measured quantitatively on radiographs. Despite their wide use in clinical practice and research, radiography and the OA grading systems are not without limitations. Radiographic images are highly dependent on the imaging angle and conditions. Therefore, both cross-sectional and longitudinal studies must take extreme care to use the same imaging conditions to avoid skewing the data. Additionally, the observed joint condition may exhibit markers that fit into different OA grades. For example, a joint may show significant subluxation but may appear to have little or no osteophytes. This creates conflict when assigning a final OA grade, and different researchers may classify the same subject differently. Nonetheless, radiographs are commonly used to determine a potential subject's ability to be included in clinical trials. Lastly, radiographs are not able to assess changes or damage to soft tissues such as the synovium, menisci, or cartilage. Other imaging modalities, such as MRI, are necessary for those assessments.

MRI provides a three-dimensional view of tissues in the body, and it is particularly useful for examining soft tissues such as menisci, cartilage, and synovium. The cost of MRIs precludes them from regular clinical use, but they are an excellent research tool for examining OA

progression. Similar to radiographs, MRI can be used for semi-quantitative and completely quantitative assessments of joints and OA progression. Semi-quantitative assessments include detailed assessments of changes to cartilage and bone conditions during OA progression. Some examples of grading systems used include the MRI OA Knee Score [18] and the Outcome Measures in Rheumatology Thumb Base OA MRI Scoring System [19] which divide the joint into subsections for evaluation as well as a wholescale evaluation. A strength of these grading systems is their detailed structure and inclusion of multiple severity groups within a particular OA grade. This provides finer classifications of OA severity and enables a more complex understanding of how different factors change and interact as OA progresses. Quantitative assessments using MRI include measuring size, shape, thickness, and volume of cartilage, bone, menisci, and cysts. In addition to the previously mentioned morphological MRI measures, compositional MRIs can be used to assess structural and biochemical changes in cartilage that occur before morphological changes are distinguishable. Compositional MRIs can also examine changes that occur beyond the most severe OA grades. For every MRI scan, care must be taken when defining the imaging specifications. Specific imaging pulse sequences are required to adequately examine different pathological features. Otherwise, artifacts from one pulse sequence could be misinterpreted as a pathologic condition. In addition to concerns over imaging specifications, MRI studies have some other limitations. One limitation of several MRI studies is that they do not occur while the joints are loaded. Imaging unloaded joints misses potential indications of OA development or progression. Image quality and consistent joint orientation are also limitations of some MRI-based research due to the varying composition and structure of joint tissues.

In addition to radiography and MRI, other imaging modalities that have been used in

joint research are ultrasound, positron emission tomography (PET)-MRI, and PET-computed tomography (CT). Ultrasound is most commonly used in the hand due to its limited ability to visualize deeper tissues. It is only able to visualize the outside of bony structures, so it is used to assess factors such as tissue inflammation, vascularity, and synovial hypertrophy. PET-MRI and PET-CT are novel techniques that can potentially provide examinations of metabolic and morphologic biomarkers, such as sites of active inflammation and increased metabolism, in early OA. However, both of these techniques currently require more evidence to prove their feasibility. Other research techniques such as in vitro, ex vivo, and in vivo studies of cells and tissues can supplement imaging research. In vitro, ex vivo, and in vivo studies can be used for more direct examinations of biochemical changes that contribute to OA initiation, OA progression, and how to treat OA.

2.2.2 In Vitro, Ex Vivo, and In Vivo Studies

In vitro models provide the ability to directly test and observe cells and cell cultures under a variety of conditions related to OA. They are among the most basic types of experimental models, and there are several types of in vitro models. One in vitro modeling method used for OA research is monolayer models. Monolayer models examine one type of cell such as chondrocytes or osteoblasts under various conditions. This method has several strengths which include low financial costs, the ability to rigidly control the cell environment, and equal access to growth media for all the cells in a culture. Monolayer models are useful for cellular level examinations such as individual cell signaling pathways and protein expression. However, they possess several limitations such as increased cost for non-immortalized cell lines, growth conditions which affect cell differentiation and growth and do not reflect the in vivo environment, restrictions on the direction of cell growth, and a limited ability to analyze cell-cell

and cell-extracellular matrix (ECM) interactions. A second in vitro modeling method is co-culturing cells. Co-culturing builds off the monolayer model by including multiple cell types in the cell culture. Multiple cell types within the same culture allows for an analysis of cell-cell interactions. Co-culture models share several limitations with monolayer models. Additionally, they require different culturing conditions for each cell type which can affect the differentiation of cells within the culture. A third in vitro modeling method is three-dimensional cell cultures either with or without scaffolds. Scaffolds provide a base upon which cells can proliferate in all directions, produce ECM, and complete other activities that create cellular interactions and tissue growth. Scaffolds are highly adjustable which allows for numerous variations that can impact model results. Additionally, scaffolds may not have the same structural integrity as in vivo conditions which can affect cell growth and interactions. Three-dimensional cultures without a scaffold typically form as pellets or spheres. Both types of three-dimensional cell cultures enable analyses of cell-cell interactions, cell-ECM interactions, and the effects of physical loads. However, limitations for three-dimensional cell cultures include slower cell proliferation rates than two-dimensional cultures, high financial costs, and uneven exposure to growth media within the culture. Other modeling methods, such as ex vivo models, can be used to address some of the limitations of in vitro models that are due to their two-dimensional or limited three-dimensional nature.

Ex vivo models are created from cell and tissue explants from a living organism. Tissue explants are a common model for OA research, and they are useful because they eliminate the difficulties associated with creating and maintaining two-dimensional or three-dimensional cell cultures. They also provide greater complexity that more closely resembles the in vivo environment. Explant models have several strengths which include cells existing within a three-

dimensional environment, they enable analyses of natural cell-cell and cell-ECM interactions, and they are simple. However, their results are influenced by cell death on the outer edges of the specimen. Additionally, tissue sources from an individual are limited, results from different sources can show noticeable variability, they are more financially costly compared to monolayer in vitro experiments, they are difficult to maintain over time, and removal from their in vivo environment reduces the biological complexity by eliminating communication with other tissues and cells. In vivo models can address some of these limitations while also providing an increase in model complexity.

In vivo models, e.g. animal models, are a useful tool for understanding OA pathogenesis and progression. There is not a gold standard for an animal model that can represent all aspects of OA within reasonable costs. Both small and large animals are used in OA research. Small animals such as rodents, rabbits, and guinea pigs are less expensive to handle, but the size of their joints is obviously much smaller than human joints and bear less of an anatomical resemblance. Therefore, they are commonly used for first-line studies of new therapeutic treatments and drugs. Larger animals such as dogs, sheep, goats, and horses are more suited for studies of OA's pathological process due to greater anatomical similarities, and they are naturally able to develop primary and secondary OA. However, they have a higher financial cost and require greater ethical considerations. Animal models can be categorized into several categories. The first category is those with naturally occurring OA. These animals are found to naturally develop OA and can be used to study OA initiation and progression, but they are costly due to the length of time that is necessary to collect results. Animals used in this type of study include rabbits, dogs, mice, guinea pigs, and horses. A second category of animal models is genetically modified models. These can be used to examine how genetic factors affect OA pathogenesis, but

they are financially expensive and can produce cartilage abnormalities along with sometimes lethal gene deletion. Animals in this type of study include mice and zebrafish. A third category of animal models is non-invasive models which use mechanical impacts to induce OA. These studies are able to look at early and advanced stages of OA by adjusting the applied loads. Other strengths include their reproducibility and their low risk of introducing infection. However, the necessary equipment is not widely available and multiple loading cycles are usually necessary to induce severe OA. The final category of animal models is invasive models. These are models that use either surgical or chemical methods to induce OA. Surgical methods commonly include transection of the anterior oblique ligament or destabilization of the medial meniscus. Strengths of surgical methods include a shorter timeframe for studies and the ability to study different stages of the disease along with therapeutic treatments. However, surgical intervention does not necessarily reflect joint changes due to degenerative OA and it can introduce infection. Chemical intervention methods are less invasive than surgical methods, can induce rapid development of OA, and are easy to reproduce. Therefore, they are useful for short-term studies. However, they can introduce widespread cell death and atypical joint changes.

The sometimes unpredictable and invasive nature of several experimental techniques is a critical limitation. Disruption or removal of cells or tissues can introduce alterations that cause their responses to no longer accurately reflect what would occur in vivo. Also, investigations of some research questions may not be plausible using the previously mentioned imaging and experimental methods. Computational studies offer a viable alternative that can address some imaging and experimental limitations.

2.2.3 Computational Studies

Computational modeling techniques allow researchers to investigate biomechanical or other situations without disruption of the in vivo environment, and they can provide examinations ranging from the cellular level to entire joints. The computational techniques used in OA research include data-driven approaches, gene regulatory network models, musculoskeletal models, multiscale models, and finite element models.

Data-driven approaches do not rely on physics-based calculations. Instead, they use provided data to predict different outcomes such as likelihood to develop OA. Input data can consist of age, sex, body mass index, physical activity levels, ethnicity, and numerous other factors. These types of models can be used to help identify which factors are more likely to affect specific outcomes, but they are unable to provide insights into the biomechanical responses of joints. Gene regulatory network models provide a method to study how genetic expression is affected by different stimuli. These models can be either qualitative or quantitative. Gene regulatory network models are useful for studying the cascade of events that can lead to cartilage degeneration, but they are limited to the cellular level and unable to answer questions at a macroscopic level. Musculoskeletal models are one type of model that is able to investigate questions on a macroscopic level. Input data for musculoskeletal models typically consists of motion marker data and ground reaction forces, and outputs for these models can include joint angles, moments, and forces. These outputs are useful for predicting which activities and circumstances may cause overloaded joints. Musculoskeletal models are only able to provide a wholistic view of joints, so they are unable to determine how different loading profiles affect contact and pressure distributions within joints. Additionally, they usually rely on generalized geometries whose dimensions may be adjusted to fit subject-specific sizes. The use of

generalized geometries limits the model's ability to provide subject-specific outcomes and insights. The use of subject-specific geometries is possible for musculoskeletal models, but they can be time-consuming and labor-intensive to create. Multiscale modeling is another technique that combines some of the strengths of cellular level and musculoskeletal models. Multiscale modeling enables analyses of how mechanical factors on the joint level affect processes on the cellular level. Typically, these models work in one direction from the macro to the micro scale in order to reduce the computational intensity. However, this prevents dynamic analyses of tissue responses by not accounting for changing tissue properties due to loading profiles or damage.

Each of the previously mentioned computational techniques have particular strengths for investigating different aspects of OA, but they are also all limited in their ability to provide detailed insights into the biomechanical environment within joints on a macroscopic level. Finite element analysis (FEA) is another computational technique that is useful for investigating joint biomechanics in relation to OA by enabling analyses of strain, stress, and contact mechanics within joints and joint tissues. The complexity of FEA allows for investigations into different scenarios related to OA. FEA also requires great attention to detail concerning model components.

2.3 What is Finite Element Analysis?

2.3.1 General Overview of Finite Element Analyses

Physical phenomena such as strain, stress, and contact between materials can be described using differential equations. FEA utilizes the finite element method (FEM) to compute approximate solutions to selected differential equations under a given set of boundary conditions. Boundary conditions for models include force or pressure loads placed on model surfaces and defining displacements of specific model sections. For the case of deformable solids, the

principle of virtual work is used as the governing equation of model behavior [20]:

$$\delta W = \int_V \boldsymbol{\sigma} : \delta \mathbf{d}\, dV - \int_V \mathbf{f} \cdot \delta \mathbf{v}\, dV - \int_{\partial V} \mathbf{t} \cdot \delta \mathbf{v}\, dA = 0 \qquad (2.1)$$

In Equation 2.1, $\boldsymbol{\sigma}$ is the Cauchy (or true) stress tensor, $\boldsymbol{\delta d}$ is the virtual rate of deformation tensor, $\mathbf{f}$ represents the body forces, $\boldsymbol{\delta v}$ represents a virtual velocity, $\mathbf{t}$ represents the surface forces, V represents the volume of the object in a deformed configuration, and ∂V represents the surface of the object in the deformed configuration. Nonlinear equations in their strong form can be extremely difficult or impossible to exactly solve over the entire model domain, so the domain is divided into smaller sub-domains called elements over which a modified form, properly called the weak form, of the governing equation is considered. Equation 2.1 represents the weak form which is used for FEA. Several definitions and inputs are required for each FEA model. Manipulation of the weak form of the governing equation and consideration of model inputs define the terms of the general formula for the FEA solution process:

$$Ku = F \qquad (2.2)$$

In Equation 2.2, K is the stiffness matrix which is influenced by material parameters and constitutive relationships. It generally represents a resistance to change in deformation (for solid mechanics). F is the combination of body and surface forces that are defined by the user before the solution process or algorithms during the solution process. The symbol u represents the nodal displacements (for solid mechanics), and this is what the model seeks to determine. Inputs and definitions for FEA can be categorized into four components. These are the model geometry, boundary conditions, definition of contact, and definition of constitutive material models.

2.3.2 Overview of Model Geometries, Element Types, and Boundary Conditions

Model geometries are the objects upon which boundary conditions and other inputs will be placed. Bones, cartilage, and other soft tissues are common objects used in biomechanical

FEAs. Generalized model geometries can be used for simulations, but subject-specific geometries provide greater anatomic detail and offer more specific insights. Subject-specific geometries can be created from imaging data such as MRI or CT scans. Calculation of outputs such as strain and stress over the entire domain of the geometry is extremely difficult or impossible, so the domain is divided into numerous sub-domains called elements. Common 3D elements are the tetrahedral element and the hexahedral element (Figure 2.4).

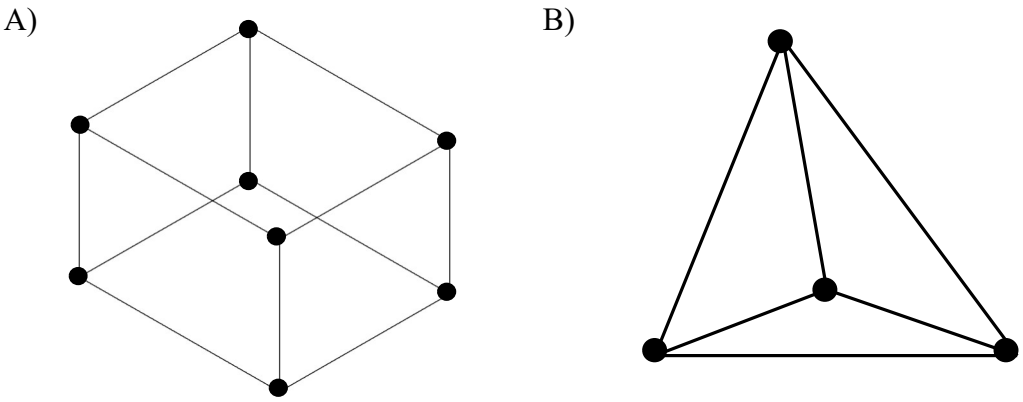

Figure 2.4. Common elements used in FEA. (A) Hexahedral element with eight nodes. (B) Tetrahedral element with four nodes.

The dots on the element corners in Figure 2.4 are called nodes. These are discrete points where certain field variables such as displacement, a crucial variable for solid mechanics analyses, are calculated. Nodal displacement is used for calculations of strain and stress at specific points within elements called integration points. Nodes are also where force and displacement boundary conditions are defined. Displacement of a node can be restricted in one or multiple directions, or it can be prescribed in specific directions. Loads can be prescribed to specific nodes, or they can be distributed along a surface of an object. Distributed loads on a surface are actually proportioned amongst the nodes. Displacement and force boundary conditions can cause objects to come into contact with each other or one object to contact itself during a simulation.

2.3.3 Overview of Model Contact

FE software does not know a priori which surfaces may come into contact as a result of force or displacement boundary conditions. If contact is expected, the contact surfaces and the nature of their interaction must be specified. There are several formulations for contact. For example, a common contact definition between articular surfaces is frictionless sliding contact. This allows the surfaces to separate and move past each other. Different FEA software packages, such as ABAQUS and FEBio, may have slight differences for similar contact definitions. Contact is a constraint on the model and it contributes additional surface forces. This increases model complexity, but contact may be a desired situation. Nodes also used for the calculation of contact mechanics between surfaces such as contact area, contact pressure, and contact force. Calculation of other field variables within an object, such as strain and stress, depend on the deformation and the chosen constitutive relationships for strain and stress.

2.3.4 Overview of Constitutive Relationships

Constitutive relationships define how two physical quantities relate to each other. In solid mechanics, a relationship between stress and strain is often defined for a material. The relationship can be linear or nonlinear. Linear constitutive relationships offer simpler model definitions and implementation, but they may not completely or accurately capture the complexity of tissue responses to loading in all situations. Nonlinear constitutive relationships may offer a better representation of a material's behavior, but they increase model complexity and computational requirements. This could affect a model's ability to converge on a solution. Another consideration for determining which constitutive relationship to use is the nature of loading. Several materials exhibit linear elastic behavior under instantaneous loading, so simpler linear constitutive relationships may be warranted over nonlinear relationships. Careful

consideration of literature concerning experimental material characterization and previous modeling practices is necessary when choosing and implementing model constitutive relationships.

2.3.5 FEA in Biomechanics Research of the Knee and Thumb

The flexibility of FEA allows it to be an effective tool for researchers investigating disease states within the knee and thumb. Specific conditions in the knee, such as the development of subchondral bone cysts (SBCs), are difficult to study experimentally for several reasons. For example, severe disruption of soft tissues supporting the knee would be necessary to access SBCs. In the basilar thumb joint, contact mechanics are difficult or impossible to replicate or measure using in vitro and in vivo experiments. FEA can be used to enhance understanding of contact mechanics within joints due to specific loading criteria and thus assess contributions to disease initiation and progression.

2.4 Knee OA and Subchondral Bone Cysts

2.4.1 Bone Marrow Lesion and Subchondral Bone Cyst Definitions, Occurrence, and Treatments

OA in the knee is the third most commonly cited musculoskeletal disorder behind lower back pain and neck pain [21]. Bone marrow lesions (BMLs) and SBCs are common co-factors of knee OA. BMLs and SBCs occur in approximately 50% of OA patients [22-24]. BMLs and SBCs are closely related, and it has been proposed that SBCs are a progression of BMLs. MRIs are commonly used to confirm the presence of BMLs and SBCs due to difficulties visualizing them on radiographs (Figure 2.5). BMLs have been defined on MRIs as ill-defined areas of high fluid signal intensity, whereas SBCs have been defined as well-delineated areas of high fluid signal intensity. Large SBCs can be identified on radiographs by a lucency with sclerotic rims in subchondral bone. These lesions can occur in both human adolescents and skeletally mature

individuals with OA [25, 26]. BMLs and SBCs have been related to localized changes in subchondral bone and degradation of articular cartilage in OA patients [27]. Early stage SBCs in adolescents generally have small amounts of cartilage damage which can increase to more severe OA over time and lead to a total joint replacement [24].

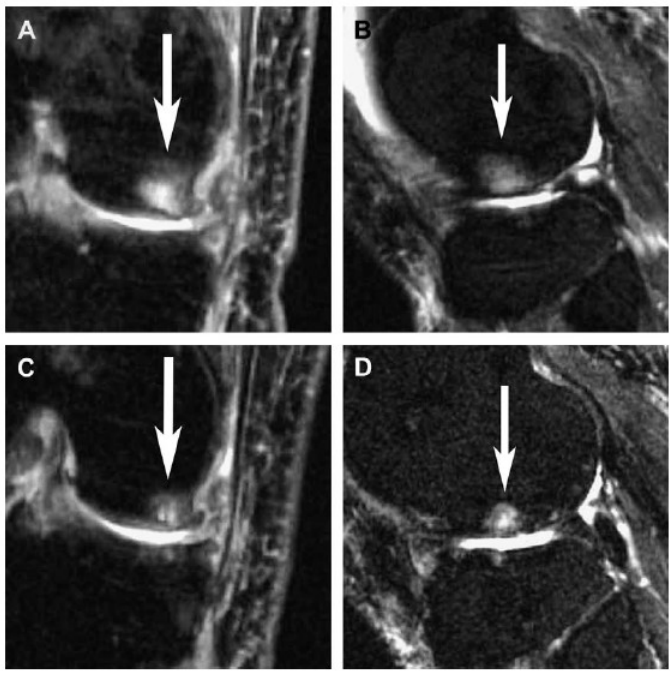

Figure 2.5. Baseline and Follow-up MRIs of a 53-year-old male patient with SBC development. (A) A baseline T2-weighted coronal view of a subchondral bone region with a bone marrow edema-like signal. (B) A baseline T2-weighted sagittal view of a subchondral bone region with a bone marrow edema-like signal. (C) A T2-weigthed coronal view MRI at 12.5 months follow-up showing development of a SBC. (D) A T2-weigthed sagittal view MRI at 12.5 months follow-up showing development of a SBC. Reproduced with permission from Carrino, JA et al., *MRI of Bone Marrow Edema-Like Signal in the Pathogenesis of Subchondral Cysts*. Osteoarthritis and Cartilage, 2006. 14(10): p. 1081-1085).

Treatment options for BMLs and SBCs include both non-surgical and surgical treatments, but there are limited options for either treatment route. Non-surgical treatments include the use of diphosphonates, prostaglandin I_2, and strontium ranelate to inhibit bone resorption and promote bone formation. Studies with diphosphonates reported reduced pain and decreased lesion sizes [28, 29]. Studies with prostaglandin I_2 also reported reduced lesion sizes [30, 31]. A

study with strontium ranelate reported both reduced lesion sizes and cartilage volume loss [32]. Braces may also be used to stabilize the joint and possibly reduce contact stresses. However, the use of braces requires greater investigation before conclusive results can be stated. Surgical treatments include subchondroplasty, high tibial osteotomy, and partial or total knee arthroplasty. Subchondroplasty is a joint-saving procedure that involves injecting a calcium phosphate bone substitute into subchondral bone that is mechanically compromised. Its purpose is to provide support to the surrounding bone and stabilize the articular cartilage. Patients that have undergone subchondroplasty have reported significant improvement in self-reported outcomes [33, 34], and up to 70% of patients did not require future arthroplasty [33]. Those that did require future arthroplasty did not usually experience complications due to the subchondroplasty [35]. High tibial osteotomy is another surgical option that aims to adjust joint alignment to offload specific areas of the knee. A limited number of studies have been reported on this procedure, but the results have indicated that patients experience satisfactory results and decreased lesion size when compared to preoperative conditions [36]. Partial or total knee arthroplasty is a surgical option once other non-operative treatment plans have been unsuccessful. Studies examining the benefits of partial and total knee arthroplasty are limited, and they have reported conflicting results. Jacobs et al compared patients undergoing either partial or total knee arthroplasty both with and without lesions [37, 38]. They reported that partial knee arthroplasty patients with lesions had lower satisfaction and smaller improvements in pain than their counterparts without lesions, but patients with a total knee arthroplasty showed greater improvements in pain than their counterparts with equivalent satisfaction levels between both groups [37]. In a separate study, Jacobs et al reported that partial knee arthroplasty patients with lesions had larger improvements in pain than their counterparts without lesions, but total knee arthroplasty patients with lesions

had smaller improvements in pain than their counterparts without lesions [38]. Given the limited lifespan of joint replacements and the invasive nature of the procedures needed to place them, more focused studies are needed to further define the benefits and necessity of knee arthroplasty when treating SBCs. Overall, increasing the understanding of SBC development and growth could contribute to the development of treatments and diagnostics that help prevent the necessity of more invasive treatments.

2.4.2 Theories of SBC Formation

Several theories detailing the formation of SBCs have been proposed. The most prominent theories are that cyst formation and growth is due to repeated mechanical trauma (mechanical trauma theory) or the presence of pressurized fluid underneath the cartilage surface and within the cyst (synovial fluid intrusion theory). The mechanical trauma theory proposes that microtrauma occurs in the subchondral bone and articular cartilage due to high impact loads or repeated loading. These loads lead to damage of the subchondral plate and inflammation which initiates cyst formation through bone necrosis. Increased stresses at the cyst boundary then drive further cyst growth. The synovial fluid intrusion theory proposes that defects in the articular cartilage allow for synovial fluid to affect the subchondral bone and initiate cyst formation and growth. Unfortunately, experimental and computational work have not provided a clear answer as to which is more likely or when elements of these theories contribute more to cyst formation and growth. Experimental and clinical research have given credence to the mechanical trauma theory [24, 39-46], and computational work has supported the experimental research [47-49]. However, experimental studies have not been able to provide direct evidence either for or against the synovial fluid intrusion theory. Histological studies have provided indirect evidence against the synovial fluid intrusion theory by reporting noticeable sclerosis, higher bone volume around

lesions, more numerous plate-like trabeculae, a thicker subchondral plate, and increased microdamage in the subchondral plate and trabeculae which suggests damage due to repeated mechanical overloading [44-46]. Arguments against the fluid intrusion theory from imaging studies include the presence of BMLs alongside SBCs and the lack of complete cartilage defects connected to every BML or SBC [24, 42, 43]. These are circumstantial arguments against the fluid intrusion theory. Some experimental work has provided indirect support for the synovial fluid intrusion theory [50-53]. Experimental attempts to directly test the synovial fluid intrusion theory are limited for several reasons. In addition to ethical concerns, any alterations to any in vivo environment would introduce severe changes that would affect the quality of any measured data. Ex vivo experiments would have concerns about true replication of the in vivo environment. Therefore, other research methodologies, such as computational methods, are necessary to understand possible contributions of synovial fluid to SBC occurrence and growth. Computational work focused on the effects of fluid pressure on SBCs is currently limited and inconclusive [54].

2.4.3 Animal Models for SBC Research

The invasive nature of experimental studies makes SBCs difficult to research in humans. Their appearance alongside OA also complicates attempts to isolate them for further fundamental understanding. An appropriate large animal model, such as a horse, can provide opportunities for us to investigate SBCs without confounding changes due to OA. SBCs occur frequently in young horses within the medial femoral condyle of the stifle joint. The stifle joint is anatomically similar to the human knee. For instance, articular cartilage thickness and subchondral bone thickness of the stifle joint show similarities to that of the human knee [55]. Such similarities between the equine stifle joint and the human knee, and the likely lack of confounding effects

due to OA, make horses a useful animal model for studying SBCs. A combination of the equine stifle joint with FEA can provide valuable insight into the effects of joint fluid on SBC occurrence and growth.

2.5 The Hand and Pipetting

2.5.1 Repetitive Tasks and Micropipette Usage

The basilar thumb joint is the second most affected joint in the hand behind the distal interphalangeal joints [10, 14]. Jobs that require repetitive tasks such as gripping, grasping, and pinching have been associated with wear on the basilar thumb joint and other joints in the hand [56-60]. Manual pipetting is a repetitive manual task that has received more attention in recent years. David and Buckle reported that workers who pipette more than 220 hours annually are more likely to report hand complaints, and workers who continuously pipette for periods longer than 30 minutes had a significantly greater chance of reporting hand complaints [61]. Björksten et al [62] conducted a study of Swedish female lab technicians and reported a higher threshold than David and Buckle. They stated that workers who pipetted more than 300 hours per year carried higher risk towards developing hand and shoulder ailments, and they reported a median yearly pipetting time of 313 hours [62]. Holm et al recently surveyed approximately 1200 female lab technicians [63]. They reported that pipetting was more closely associated with complaints than other lab tasks and that symptoms were greatest in the thumb and wrist for high weekly exposure to pipetting (> 5 hours) [63]. Manual pipetting is a repetitive task that cannot be completely avoided in many laboratory settings. Therefore, an investigation into ergonomic pipette design could help determine which design features have the greatest impact on forces in the hand and thumb during pipetting. A reduction of forces in the hand could decrease discomfort and injury due to continuous micropipette use.

2.5.2 Past Techniques Used for Study of Micropipette Design

Experimental studies have mostly sought to understand how micropipette design affects the hand and forearm through a combination of surveys/questionnaires, measurement of joint angles, and EMGs [61-73]. This information can be useful, but their results can be limited in their scope and these methods are susceptible to unavoidable issues such as personal bias in surveys, marker placement and movement relative to underlying bone in kinematic studies, and muscle signal crosstalk when collecting EMG data. Computational models have also been used to study the effects of micropipette usage on the body. Previous computational models of pipetting have focused on the estimation of joint angles, joint moments, muscle forces in the hand, forces experienced by the whole joint, and tendon displacement [74-77]. These types of models require several assumptions that may not fully capture muscle activation patterns and forces. Assumptions include generalized bone geometries, muscle attachment and size, and muscle forces derived from kinematic data. Additionally, they do not provide an insight into contact or stresses that occur within any given joint.

2.5.3 MRI-Based FEA and its Advantages

Cartilage mechanics and contact between articular surfaces are important considerations when assessing potential OA development and progression. MRI-based FEA is a computational method that can be used to analyze in vivo stresses and contact within a particular joint with minimal assumptions about boundary conditions. The minimization of boundary conditions is accomplished through the use of kinematic translations and rotations that are defined by relating an unloaded state of a given bone to its loaded state. The unloaded state of the bone is captured by a MRI scan while muscles surrounding the joint are relaxed. The loaded state of the bone is captured by a MRI scan while a subject is performing an active task such as pipetting. Scans of

the unloaded state of the bone are typically used to create model geometries due to their higher quality. The scan of the loaded state of the bone is typically shorter, and thus a lower signal to noise ratio, due to concerns of subject fatigue and motion artifacts on the images. In a given model, application of the kinematic transformation defined by the loaded and unloaded scans places a model bone in its loaded state. Afterwards, it can be manipulated to remove any initial contact with other objects and displaced to the loaded contact during model execution. This approach has been previously used in analyses of the wrist [78-80]. Another advantage of MRI-based modeling is that it allows for the use of subject specific geometries in place of generalized geometries. This maintains unique bone shapes in a given analysis which enables more specific conclusions to be drawn from subjects. Special tools are necessary to utilize MRI-based modeling. Specifically, the creation of a MRI-compatible micropipette simulator would enable the investigation of how micropipette design affects contact forces, locations, and pressures within the basilar thumb joint.

2.6 Specific Aims, Rationale, and Hypotheses/Design Goals

FEA can be used to understand mechanical contributions to musculoskeletal disease initiation and progression in the knee and hand. A greater understanding of the mechanical contributions to OA and related conditions in these joints can help clinicians and researchers develop effective treatments and improve ergonomic design of laboratory tools. The three specific aims that constitute this body of work will be organized into three chapters. The first chapter will detail work concerning SBCs within the medial femoral condyle of the equine stifle joint. The second chapter will detail the design and fabrication of a MRI-compatible micropipette simulator which will be used in the following chapter. The third chapter will detail a pilot study analyzing the effects of two micropipette design parameters.

2.6.1 Specific Aim 1

Specific Aim 1: The contributions of intra-cyst fluid to growth of SBCs within the medial femoral condyle must be examined. Compression, tension, and shear will be tracked in a region of interest surrounding cysts of three different sizes (0.03 cm^3, 0.5 cm^3, and 1 cm^3). Intra-cyst fluid will be simulated through two methods: normal forces on the inner cyst wall or the inclusion of a soft solid within the cyst cavity.

Rationale: This data will contribute to the understanding of how intra-cyst fluid pressure influences the growth of SBCs. This will increase the general knowledge of SBC formation and growth.

Hypothesis: We hypothesized that bone stresses in the soft solid models would not exceed estimated yield strengths for compression, tension, or shear. We also hypothesized that high simulated fluid pressure (using normal forces) would increase the stress in the surrounding bone to exceed estimated yield strength for either compression, tension, or shear.

2.6.2 Specific Aim 2

Specific Aim 2: A MRI-compatible modular micropipette simulator must be designed and manufactured. The proposed simulator will allow for feedback to subjects and researchers so that experimental conditions can be monitored for consistency. Modularity of the simulator will allow multiple pipette designs to be tested with minimal disruption.

Rationale: MRI-based FEA reduces the assumptions about boundary conditions compared to other modeling methods, and it enables examinations of in vivo contact mechanics. A MRI-compatible modular micropipette simulator system must be constructed to be able to utilize this modeling technique.

Design Goals: MRI-compatibility, modularity, and reproducibility of experimental conditions were the main design objectives. Ferromagnetic substances could not be included for safety concerns, and other metallic substances were excluded to avoid image distortion. Therefore, plastic materials were determined to be the most suitable. Additive manufacturing was used to fabricate the system parts. Modularity was essential to ease the transition between micropipette designs during testing.

2.6.3 Specific Aim 3

Specific Aim 3: The effects of micropipette handle diameter and the presence of a finger rest on contact mechanics in the basilar thumb joint were evaluated using MRI-based FEA. A total of six micropipette designs were fabricated using three different handle diameters (12 mm, 25 mm, and 40 mm) and the inclusion or exclusion of a finger rest. Contact location, contact force, contact area, and peak contact pressure were compared across micropipette designs.

Rationale: An initial study is necessary to demonstrate that MRI-based FEA can be used to assess differences in basilar thumb joint contact mechanics across micropipette designs. An understanding of how micropipette handle diameter, inclusion of a finger rest, or other design parameters affect basilar thumb joint contact mechanics can influence future micropipette designs.

Hypothesis: We hypothesized that increasing the micropipette handle diameter would decrease contact area, contact force, and peak contact pressures in the basilar thumb joint. We also hypothesized that the presence of a finger rest would decrease contact area, contact force, and peak contact pressure.

2.7 References

1. Cisternas, M.G., et al., *Alternative Methods for Defining Osteoarthritis and the Impact on Estimating Prevalence in a US Population-Based Survey.* Arthritis Care Res (Hoboken), 2016. **68**(5): p. 574-80.

2. Disease, G.B.D., I. Injury, and C. Prevalence, *Global, regional, and national incidence, prevalence, and years lived with disability for 354 diseases and injuries for 195 countries and territories, 1990-2017: a systematic analysis for the Global Burden of Disease Study 2017.* Lancet, 2018. **392**(10159): p. 1789-1858.

3. Murphy, L.B., et al., *Medical Expenditures and Earnings Losses Among US Adults With Arthritis in 2013.* Arthritis Care Res (Hoboken), 2018. **70**(6): p. 869-876.

4. Haugen, I.K., et al., *Prevalence, incidence and progression of hand osteoarthritis in the general population: the Framingham Osteoarthritis Study.* Ann Rheum Dis, 2011. **70**(9): p. 1581-6.

5. Zhang, Y., et al., *Prevalence of symptomatic hand osteoarthritis and its impact on functional status among the elderly: The Framingham Study.* Am J Epidemiol, 2002. **156**(11): p. 1021-7.

6. Felson, D.T., et al., *The prevalence of knee osteoarthritis in the elderly. The Framingham Osteoarthritis Study.* Arthritis Rheum, 1987. **30**(8): p. 914-8.

7. Jordan, J.M., et al., *Prevalence of knee symptoms and radiographic and symptomatic knee osteoarthritis in African Americans and Caucasians: the Johnston County Osteoarthritis Project.* J Rheumatol, 2007. **34**(1): p. 172-80.

8. Jin, Z., et al., *Incidence trend of five common musculoskeletal disorders from 1990 to 2017 at the global, regional and national level: results from the global burden of disease study 2017.* Ann Rheum Dis, 2020. **79**(8): p. 1014-1022.

9. Haugen, I.K., et al., *Prevalence, incidence and progression of hand osteoarthritis in the general population: the Framingham Osteoarthritis Study.* Annals of the rheumatic diseases, 2011. **70**(9): p. 1581-1586.

10. Wilder, F.V., J.P. Barrett, and E.J. Farina, *Joint-specific prevalence of osteoarthritis of the hand.* Osteoarthritis Cartilage, 2006. **14**(9): p. 953-7.

11. Etherington, J., et al., *The effect of weight-bearing exercise on bone mineral density: a study of female ex-elite athletes and the general population.* J Bone Miner Res, 1996. **11**(9): p. 1333-8.

12. Lester, M.E., et al., *Influence of exercise mode and osteogenic index on bone biomarker responses during short-term physical training.* Bone, 2009. **45**(4): p. 768-76.

13. Kellgren, J.H. and J.S. Lawrence, *Radiological assessment of osteo-arthrosis.* Ann Rheum Dis, 1957. **16**(4): p. 494-502.

14. Dahaghin, S., et al., *Prevalence and pattern of radiographic hand osteoarthritis and association with pain and disability (the Rotterdam study).* Ann Rheum Dis, 2005. **64**(5): p. 682-7.

15. Eaton, R.G. and J.W. Littler, *Ligament reconstruction for the painful thumb carpometacarpal joint.* J Bone Joint Surg Am, 1973. **55**(8): p. 1655-66.

16. Eaton, R.G. and S.Z. Glickel, *Trapeziometacarpal osteoarthritis. Staging as a rationale for treatment.* Hand Clin, 1987. **3**(4): p. 455-71.

17. Wolf, J.M., et al., *The carpometacarpal stress view radiograph in the evaluation of trapeziometacarpal joint laxity.* J Hand Surg Am, 2009. **34**(8): p. 1402-6.

18. Hunter, D.J., et al., *Evolution of semi-quantitative whole joint assessment of knee OA: MOAKS (MRI Osteoarthritis Knee Score).* Osteoarthritis Cartilage, 2011. **19**(8): p. 990-1002.

19. Kroon, F.P.B., et al., *Development and Reliability of the OMERACT Thumb Base Osteoarthritis Magnetic Resonance Imaging Scoring System.* J Rheumatol, 2017. **44**(11): p. 1694-1698.

20. Bonet, J. and R.D. Wood, *Nonlinear continuum mechanics for finite element analysis*. 1997: Cambridge university press.

21. March, L., et al., *Burden of disability due to musculoskeletal (MSK) disorders.* Best Pract Res Clin Rheumatol, 2014. **28**(3): p. 353-66.

22. Raynauld, J.P., et al., *Correlation between bone lesion changes and cartilage volume loss in patients with osteoarthritis of the knee as assessed by quantitative magnetic resonance imaging over a 24-month period.* Ann Rheum Dis, 2008. **67**(5): p. 683-8.

23. Wu, H., et al., *Prevalence of knee abnormalities in patients with osteoarthritis and anterior cruciate ligament injury identified with peripheral magnetic resonance imaging: a pilot study.* Can Assoc Radiol J, 2007. **58**(3): p. 167-75.

24. Tanamas, S.K., et al., *The association between subchondral bone cysts and tibial cartilage volume and risk of joint replacement in people with knee osteoarthritis: a longitudinal study.* Arthritis research & therapy, 2010. **12**(2): p. R58.

25. Audrey, H.X., H.R. Abd Razak, and T.H. Andrew, *The truth behind subchondral cysts in osteoarthritis of the knee.* Open Orthop J, 2014. **8**: p. 7-10.

26. Ghahremani, S., et al., *Osteochondral lesions in pediatric and adolescent patients.* Semin Musculoskelet Radiol, 2014. **18**(5): p. 505-12.

27. Chen, Y., et al., *Bone turnover and articular cartilage differences localized to subchondral cysts in knees with advanced osteoarthritis.* Osteoarthritis Cartilage, 2015. **23**(12): p. 2174-2183.

28. Laslett, L.L., et al., *Zoledronic acid reduces knee pain and bone marrow lesions over 1 year: a randomised controlled trial.* Ann Rheum Dis, 2012. **71**(8): p. 1322-8.

29. Varenna, M., et al., *Intravenous neridronate in the treatment of acute painful knee osteoarthritis: a randomized controlled study.* Rheumatology (Oxford), 2015. **54**(10): p. 1826-32.

30. Jäger, M., et al., *Rationale for prostaglandin I2 in bone marrow oedema--from theory to application.* Arthritis Res Ther, 2008. **10**(5): p. R120.

31. Mayerhoefer, M.E., et al., *Short-term outcome of painful bone marrow oedema of the knee following oral treatment with iloprost or tramadol: results of an exploratory phase II study of 41 patients.* Rheumatology (Oxford), 2007. **46**(9): p. 1460-5.

32. Pelletier, J.P., et al., *Disease-modifying effect of strontium ranelate in a subset of patients from the Phase III knee osteoarthritis study SEKOIA using quantitative MRI: reduction in bone marrow lesions protects against cartilage loss.* Ann Rheum Dis, 2015. **74**(2): p. 422-9.

33. Cohen, S.B. and P.F. Sharkey, *Subchondroplasty for Treating Bone Marrow Lesions.* J Knee Surg, 2016. **29**(7): p. 555-563.

34. Davis, A.T., et al., *Short-term outcomes of the subchondroplasty procedure for the treatment of bone marrow edema lesions in patients with knee osteoarthritis.* Orthopaedic Journal of Sports Medicine, 2015. **3**(7_suppl2): p. 2325967115S00125.

35. Yoo, J.Y., et al., *Knee Arthroplasty After Subchondroplasty: Early Results, Complications, and Technical Challenges.* J Arthroplasty, 2016. **31**(10): p. 2188-92.

36. Kröner, A.H., et al., *Influence of high tibial osteotomy on bone marrow edema in the knee.* Clin Orthop Relat Res, 2007. **454**: p. 155-62.

37. Jacobs, C.A., C.P. Christensen, and T. Karthikeyan, *Subchondral Bone Marrow Edema Had Greater Effect on Postoperative Pain After Medial Unicompartmental Knee Arthroplasty Than Total Knee Arthroplasty.* J Arthroplasty, 2016. **31**(2): p. 491-4.

38. Jacobs, C.A., et al., *The Location and Severity of Preoperative Subchondral Bone Marrow Lesions Were Not Associated With Inferior Postoperative Outcomes After Medial Unicompartmental Knee Arthroplasty or Total Knee Arthroplasty.* J Arthroplasty, 2016. **31**(11): p. 2476-2480.

39. Jeffcott, L.B., S.E. Kold, and F. Melsen, *Aspects of the pathology of stifle bone cysts in the horse.* Equine Vet J, 1983. **15**(4): p. 304-11.

40. Ray, C.S., et al., *Development of subchondral cystic lesions after articular cartilage and subchondral bone damage in young horses.* Equine Vet J, 1996. **28**(3): p. 225-232.

41. Verschooten, F. and A. De Moor, *Subchondral cystic and related lesions affecting the equine pedal bone and stifle.* Equine Vet J, 1982. **14**(1): p. 47-54.

42. Crema, M.D., et al., *Subchondral cystlike lesions develop longitudinally in areas of bone marrow edema-like lesions in patients with or at risk for knee osteoarthritis: detection with MR imaging--the MOST study.* Radiology, 2010. **256**(3): p. 855-62.

43. Carrino, J., et al., *MRI of bone marrow edema-like signal in the pathogenesis of subchondral cysts.* Osteoarthritis and cartilage, 2006. **14**(10): p. 1081-1085.

44. Muratovic, D., et al., *Bone marrow lesions detected by specific combination of MRI sequences are associated with severity of osteochondral degeneration.* Arthritis Res Ther, 2016. **18**: p. 54.

45. Muratovic, D., et al., *Bone marrow lesions in knee osteoarthritis: regional differences in tibial subchondral bone microstructure and their association with cartilage degeneration.* Osteoarthritis Cartilage, 2019. **27**(11): p. 1653-1662.

46. Muratovic, D., et al., *Bone matrix microdamage and vascular changes characterize bone marrow lesions in the subchondral bone of knee osteoarthritis.* Bone, 2018. **108**: p. 193-201.

47. Frazer, L.L., E.M. Santschi, and K.J. Fischer, *The impact of subchondral bone cysts on local bone stresses in the medial femoral condyle of the equine stifle joint.* Med Eng Phys, 2017. **48**: p. 158-167.

48. McErlain, D.D., et al., *Subchondral cysts create increased intra-osseous stress in early knee OA: A finite element analysis using simulated lesions.* Bone, 2011. **48**(3): p. 639-46.

49. Shirazi, R. and A. Shirazi-Adl, *Computational biomechanics of articular cartilage of human knee joint: effect of osteochondral defects.* J Biomech, 2009. **42**(15): p. 2458-65.

50. Kold, S.E., J. Hickman, and F. Melsen, *An experimental study of the healing process of equine chondral and osteochondral defects.* Equine Vet J, 1986. **18**(1): p. 18-24.

51. Reilingh, M.L., et al., *Morphological analysis of subchondral talar cysts on microCT.* Knee Surg Sports Traumatol Arthrosc, 2013. **21**(6): p. 1409-17.

52. Landells, J.W., *The bone cysts of osteoarthritis.* J Bone Joint Surg Br, 1953. **35-b**(4): p. 643-9.

53. Crema, M., et al., *Contrast-enhanced MRI of subchondral cysts in patients with or at risk for knee osteoarthritis: the MOST study.* European journal of radiology, 2010. **75**(1): p. e92-e96.

54. Cox, L.G., et al., *The role of pressurized fluid in subchondral bone cyst growth.* Bone, 2011. **49**(4): p. 762-8.

55. Frisbie, D.D., M.W. Cross, and C.W. McIlwraith, *A comparative study of articular cartilage thickness in the stifle of animal species used in human pre-clinical studies compared to articular cartilage thickness in the human knee.* Vet Comp Orthop Traumatol, 2006. **19**(3): p. 142-6.

56. Winzeler, S. and B.D. Rosenstein, *Occupational injury and illness of the thumb. Causes and solutions.* Aaohn j, 1996. **44**(10): p. 487-92.

57. Haara, M.M., et al., *Osteoarthritis of finger joints in Finns aged 30 or over: prevalence, determinants, and association with mortality.* Ann Rheum Dis, 2003. **62**(2): p. 151-8.

58. Rossignol, M., et al., *Primary osteoarthritis of hip, knee, and hand in relation to occupational exposure.* Occup Environ Med, 2005. **62**(11): p. 772-7.

59. Solovieva, S., et al., *Hand use and patterns of joint involvement in osteoarthritis. A comparison of female dentists and teachers.* Rheumatology (Oxford), 2005. **44**(4): p. 521-8.

60. Rossignol, M., et al., *Primary osteoarthritis and occupations: a national cross sectional survey of 10 412 symptomatic patients.* Occup Environ Med, 2003. **60**(11): p. 882-6.

61. David, G. and P. Buckle, *A questionnaire survey of the ergonomie problems associated with pipettes and their usage with specific reference to work-related upper limb disorders.* Applied Ergonomics, 1997. **28**(4): p. 257-262.

62. Björksten, M.G., B. Almby, and E.S. Jansson, *Hand and shoulder ailments among laboratory technicians using modern plunger-operated pipettes.* Appl Ergon, 1994. **25**(2): p. 88-94.

63. Holm, J.W., O.S. Mortensen, and F. Gyntelberg, *Upper limb disorders among biomedical laboratory workers using pipettes.* Cogent Medicine, 2016. **3**(1): p. 1256849.

64. Asundi, K.R., J.M. Bach, and D.M. Rempel, *Thumb force and muscle loads are influenced by the design of a mechanical pipette and by pipetting tasks.* Hum Factors, 2005. **47**(1): p. 67-76.

65. Fredriksson, K., *Laboratory work with automatic pipettes: a study on how pipetting affects the thumb.* Ergonomics, 1995. **38**(5): p. 1067-73.

66. Kim, E., F. Aqlan, and A. Freivalds, *Development of an ergonomic four-finger-push manual pipette design.* Appl Ergon, 2020. **85**: p. 103045.

67. Lee, Y.H. and M.S. Jiang, *An ergonomic design and performance evaluation of pipettes.* Appl Ergon, 1999. **30**(6): p. 487-93.

68. Lichty, M.G., I.L. Janowitz, and D.M. Rempel, *Ergonomic evaluation of ten single-channel pipettes.* Work, 2011. **39**(2): p. 177-85.

69. Maija, L. and N. Nina, *Ergonomics and the usability of mechanical single-channel liquid dosage pipettes.* International Journal of Industrial Ergonomics, 2006. **36**(3): p. 257-263.

70. Ming-Lun, L., et al., *An investigation of hand forces and postures for using selected mechanical pipettes.* International Journal of Industrial Ergonomics, 2008. **38**(1): p. 18-29.

71. Park, J.K. and B. Buchholz, *Effects of work surface height on muscle activity and posture of the upper extremity during simulated pipetting.* Ergonomics, 2013. **56**(7): p. 1147-58.

72. Rempel, P., et al., *The effect of two alternative arm supports on shoulder and upper back muscle loading during pipetting.* Work, 2011. **39**(2): p. 195-200.

73. Sormunen, E. and N. Nevala, *User-oriented evaluation of mechanical single-channel axial pipettes.* Appl Ergon, 2013. **44**(5): p. 785-91.

74. Wu, J.Z., et al., *Inverse dynamic analysis of the biomechanics of the thumb while pipetting: a case study.* Med Eng Phys, 2012. **34**(6): p. 693-701.

75. Wu, J.Z., et al., *Analysis of the musculoskeletal loading of the thumb during pipetting--a pilot study.* J Biomech, 2014. **47**(2): p. 392-9.

76. Wu, J.Z., et al., *The musculoskeletal loading profile of the thumb during pipetting based on tendon displacement.* Med Eng Phys, 2013. **35**(12): p. 1801-10.

77. Wu, J.Z., et al., *Analysis of the Constraint Joint Loading in the Thumb During Pipetting.* J Biomech Eng, 2015. **137**(8): p. 084501.

78. Johnson, J.E., et al., *Computationally efficient magnetic resonance imaging based surface contact modeling as a tool to evaluate joint injuries and outcomes of surgical interventions compared to finite element modeling.* J Biomech Eng, 2014. **136**(4): p. 0410021-9.

79. Modaresi, S., et al., *Evaluation of midcarpal capitate contact mechanics in normal, injured and post-operative wrists.* Clin Biomech (Bristol, Avon), 2017. **47**: p. 96-102.

80. Pillai, R.R., et al., *MRI-based modeling for evaluation of in vivo contact mechanics in the human wrist during active light grasp.* J Biomech, 2007. **40**(12): p. 2781-7.

3. Effects of Internal Fluid Pressure on Stresses in Subchondral Bone Cysts of the Medial Femoral Condyle

Manuscript submitted to Annals of Biomedical Engineering

Accepted for publication October 2021

Running Title: Fluid Pressure and Cyst Growth

Nolan M. Norton[A], MS

Elizabeth Santschi[B], DVM, Diplomate ACVS

Kenneth J. Fischer[A,C,D], PhD

[A]The University of Kansas, Bioengineering Program

[B]Kansas State University, College of Veterinary Medicine

[C]The University of Kansas Medical Center, Orthopedics and Sports Medicine

[D]The University of Kansas, Mechanical Engineering

The corresponding author is Dr. Fischer

3.1 Abstract

The etiology of subchondral bone cysts (SBCs) is not fully understood. Mechanical trauma and fluid pressure are two mechanisms believed to cause their formation and growth. The equine stifle joint provides a natural animal model for studying SBCs. Computed tomography images of an extended yearling cadaveric stifle joint were segmented using ScanIP to isolate bones and relevant soft tissues. Three model geometries were created to simulate cyst sizes of approximately 0.03 cm^3 (C1), 0.5 cm^3 (C2), and 1 cm^3 (C3). A uniform pressure resulting in 3000N force was applied at the proximal end of the femur. Two types of simulations, filled-cyst and empty-cysts with uniform pressure loads, were used to simulate fluid pressurization. Our models suggest that shear stresses are likely the cause of failure for the subchondral bone and not pressurized fluid from the joint. Bone stresses did not begin to increase until cyst pressures were greater than 3 MPa. Comparison of bone stresses to estimated yield strengths for trabecular bone indicated that shear stresses were the most likely to cause bone damage. Synovial fluid pressure acts upon a porous trabecular bone network, soft tissue, and marrow, so the continuum nature of our model likely overestimates the predicted effects of fluid pressures.

Key Words: Intra-cyst Fluid, Pressure, Bone Stress, Equine Stifle Joint, Finite Element Analysis

3.2 Introduction

A subchondral bone cyst (SBC) can occur in both human adolescents and skeletally mature individuals with osteoarthritis [1, 2]. Early stage SBCs in adolescents generally have small amounts of cartilage damage which can increase to more severe osteoarthritis over time and lead to a total joint replacement [3]. The invasive nature of experimental studies makes SBCs difficult to research in humans. An appropriate large animal model, such as a horse, allows us to investigate SBCs and possible future clinical treatments. SBCs occur frequently in young horses within the medial femoral condyle of the stifle joint which is anatomically similar to the human knee. For instance, articular cartilage thickness and subchondral bone thickness of the stifle joint is similar to that of the human knee [4]. Such similarities between the equine stifle joint and the human knee make horses a useful animal model for studying SBCs.

Mechanical trauma and pressurized synovial fluid have been proposed as causes for SBC initiation and growth. The mechanical trauma theory proposes that microtrauma occurs in the subchondral bone and articular cartilage due to a high impact load or repeated high loading. This leads to damage to the subchondral plate and inflammation which initiates cyst formation. Increased stresses at the cyst boundary then drive further cyst growth. Experimental and clinical research has given credence to this theory [5-7] and computational work has supported the experimental research [8-10]. The pressurized synovial fluid theory proposes that defects in the articular cartilage allow for synovial fluid to affect the subchondral bone and initiate cyst formation and growth. Experimental work has provided indirect support for this theory [11-13]. Computational work focused on the effects of fluid pressure in SBCs is currently limited [14].

Computational studies can be an asset when determining the effects of fluid pressure on subchondral bone. They can be used to overcome inherent experimental difficulties and

limitations such as the alterations of the in vivo environment that are necessary to record data. We utilized two approaches to determine the effects of fluid pressure on stresses in the bone surrounding the cysts. Due to the unknown magnitude of pressures within SBCs, our first approach was to perform a parametric analysis of applied normal pressures on the inner surface of an empty cyst. Our second approach was to fill the cyst with material to represent intra-cyst fluid. Both of these approaches were used for three different sizes of SBC. We hypothesized that bone stresses in the filled-cyst models would not exceed estimated yield strengths for compression, tension, or shear. We also hypothesized that high simulated fluid pressure would increase the stress in the surrounding bone to exceed estimated yield strength for either compression, tension, or shear.

3.3 Materials and Methods

3.3.1 Segmentation and Meshing

The models used in this study were modified versions of models from previously published studies of SBCs in the medial femoral condyle of the equine stifle joint [8, 15]. Computerized tomography (CT) images of a cadaveric yearling thoroughbred's extended stifle joint were imported into Simpleware ScanIP (Synopsis, Inc) for manual segmentation and meshing. The femur, tibia, patella, articular cartilage, menisci, patellar ligaments, and posterior cruciate ligament were isolated to create a three-dimensional representation of the joint. A soft tissue window was used during segmentation to help identify the soft tissue boundaries of the ligaments and menisci. Ligaments were segmented through a combination of identifying their insertion points and following tissue outlines on the CT data. Articular cartilage was assumed to have a thickness of two millimeters [16]. This was achieved through dilation of the bone by two millimeters to create a uniform surface. The thickness of cartilage was increased to 2.5-3.0

millimeters on the axial portions of the medial femoral condyle to match anatomical observations. Articular cartilage completely covered the SBC openings and was left intact. Tissue boundaries on the CT images and visual aids from available anatomical specimens were used in combination to segment the menisci between the articular surfaces. A professor of veterinary surgery was involved in the segmentation process to provide guidance and detailed feedback on anatomical features (Figure 3.1).

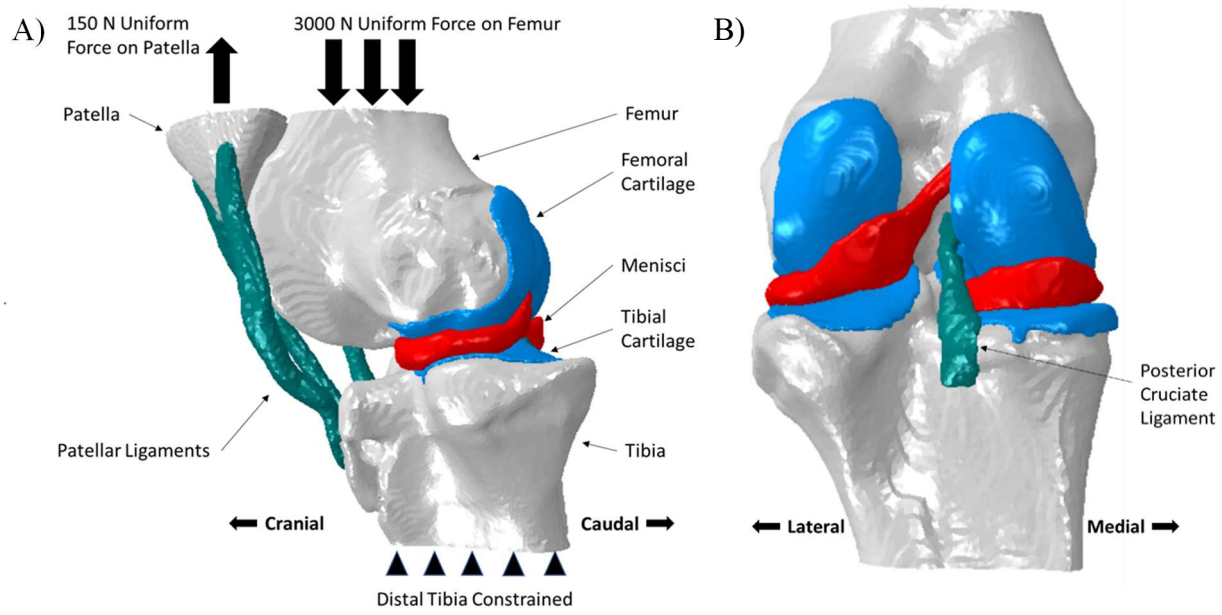

Figure 3.1. (A) Medial view of the fully assembled model. (B) Caudal view of the fully assembled model.

Three different models with cyst sizes of approximately 0.03 cm^3 (C1), 0.5 cm^3 (C2), or 1 cm^3 (C3) were used for this study (Figure 3.2). The 3D geometries were meshed with 4-node tetrahedral elements (C3D4) using ScanIP's +FE Free meshing algorithm. A region of interest (ROI) was defined around the bone cysts where bone stresses were calculated. The mesh quality for the ROI surrounding each cyst was checked, and there were not any concerning deviations from optimally shaped elements (Appendix A.1). The resulting geometries were then imported into Abaqus 2017 (Dassault Systemes) where material properties and boundary conditions were defined.

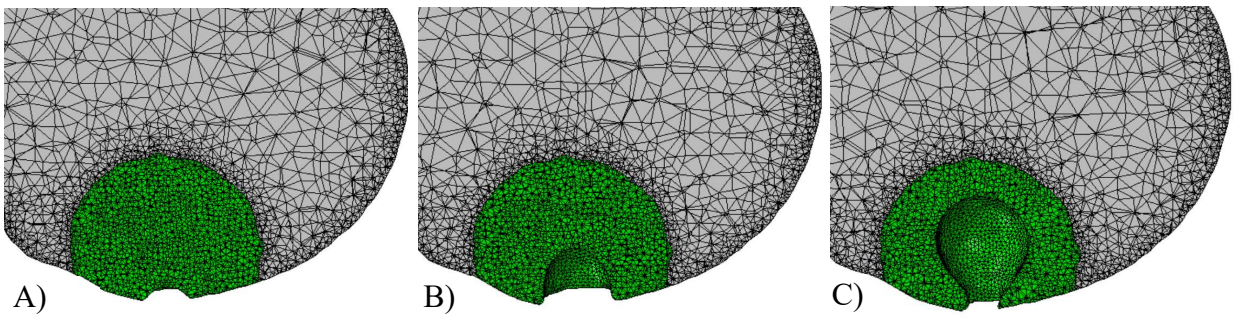

Figure 3.2. (A) C1 Cyst.(B) C2 Cyst. (C) C3 Cyst from a para-sagittal section of the distal medial femoral condyle. The green region around the cyst is the ROI where bone stresses were calculated.

3.3.2 Material Properties

The modulus of bone tissue is dependent on its mass density [17-20], so the model included 20 levels of bone tissue properties. The Young's modulus of bone tissue was related to the CT Hounsfield unit using Equations (3.1) and (3.2):

$$Apparent\ Density\ = (1.067 * 10^{-3}) * HU \qquad (3.1)$$

$$Young's\ Modulus\ (MPa) = (6.0 * 10^{3}) * Apparent\ Density^{2.5} \quad (3.2)$$

The power of 2.5 was used because Young's modulus is proportional to ρ^2 for low density bone and proportional to ρ^3 for high density bone [17, 20, 21]. These equations resulted in Young's moduli for bone ranging from 50 MPa to 21,000 MPa. Poisson's ratio for the bone tissue was set at 0.3. The cartilage and ligaments were assumed to be linear and isotropic with nearly incompressible behavior (Table 3.1). Cartilage properties were adapted from Laasanen et al [22]. Ligament properties were adapted from Butler et al [23]. The anterior cruciate ligament and collateral ligaments were not included in the models because they were not loaded in tension during the simulation with a compressive load. The menisci were modeled as linear and anisotropic to account for their aligned collagen structure. Meniscal properties were adapted from Donahue et al. [24] and Tissakht et al. [25], and they were assigned in the radial,

circumferential, and axial directions. The cyst filling was modeled as isotropic with nearly incompressible behavior. Young's modulus for the cyst filling was determined from the relationship between a bulk modulus of 2.15 GPa, which is similar to that of water, and Poisson's ratio in Equation (3.3).

$$Young's\ Modulus\ (MPa) = 3 * Bulk\ Modulus\ (MPa) * (1 - 2 * Poisson's\ Ratio) \quad (3.3)$$

Table 3.1. Material Properties

Structure	Type	Young's Mod (MPa)	Poisson Ratio
Bone	Iso.	50-21,000	0.3
Menisci	Aniso.	Radial, Axial = 20 Circumferential = 120	Radial, Axial = 0.3 Circumferential = 0.45
Cartilage	Iso.	25	0.45
Ligaments	Iso.	300	0.45
Cyst Filling	Iso.	64.5	0.495

3.3.3 Boundary Conditions

The menisci were constrained through ties to their anatomical insertion points. Additionally, the peripheral rim of each meniscus was attached to the tibial plateau through four springs (k=10 N/mm). ABAQUS's general contact formulation with frictionless, non-linear surface-to-surface contact was used in all three models. All three translations of the distal tibia were constrained. Flexion/extension and internal/external rotation of the femur were also constrained. A uniform pressure was applied across the proximal surface of the partial femur, resulting in a 3000 N compressive joint force. This force is likely a conservative estimate of the load placed on the stifle joint during light exercise. A uniform tension resulting in a 150 N force was applied on the proximal end of the patella to provide additional stabilization. A literature search by the authors did not produce any reported synovial fluid pressure values within the equine stifle joint. For the uniform cyst pressure portion of the study, a parametric approach with

order(s) of magnitude increases was used in our simulations. Normal pressures of 0 Pa, 1 kPa, 100 kPa, 1 MPa, 3 MPa, 5 MPa, and 10 MPa were applied to the inner surface of the empty cysts to simulate possible intra-cyst fluid pressures.

3.3.4 Stress Analysis

Custom Matlab code was used to analyze the bone stress data from the ROI surrounding the cyst for compression, tension, and shear. Compression was taken to be only the negative values of the third principal stress. Compression was presented as positive (magnitude) values for consistency and comparison of bone stress results. Tension was taken to be only the positive values of the first principal stress. Shear was taken to be half of the maximum tresca stress. First, all zero values were filtered out of the data. Then the average of stresses above the 99^{th} percentile of stress magnitude was calculated for tension, compression, and shear data to represent peak values for those bone stresses. In the filled-cyst models, cyst pressure values were tracked for both the cyst filling and elements along the inner surface of the cyst. Pressure values were calculated as the negative (opposite) of the hydrostatic stress (mean normal stress) of the stress tensor.

3.4 Results

Peak bone stress did not change for any cyst size with applied normal cyst pressures ≤ 100 kPa (Figure 3.3). Therefore, stresses at the cyst pressure of 100 kPa were used to assess relative changes in stress measures at greater normal pressures. Increased tensile stress was predicted with cyst pressure ≥ 3 MPa for C2 and C3, whereas notably increased shear stress was only predicted with a normal pressure of 10 MPa for all cyst sizes.

A)

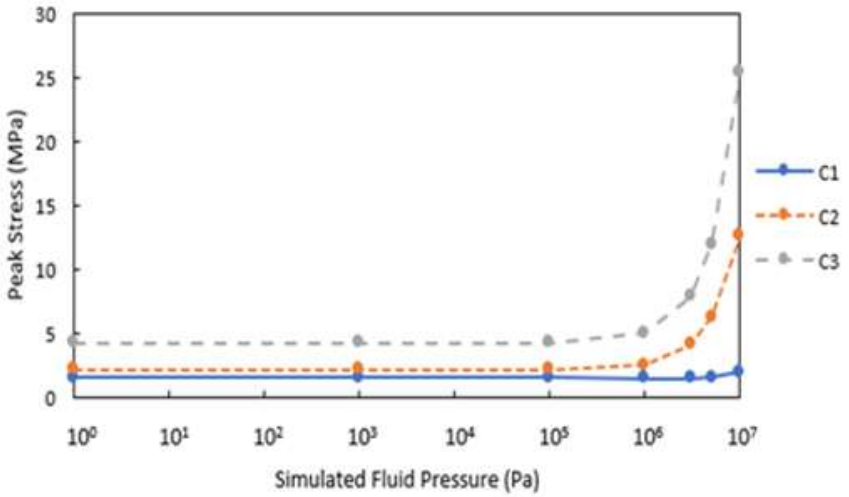

B)

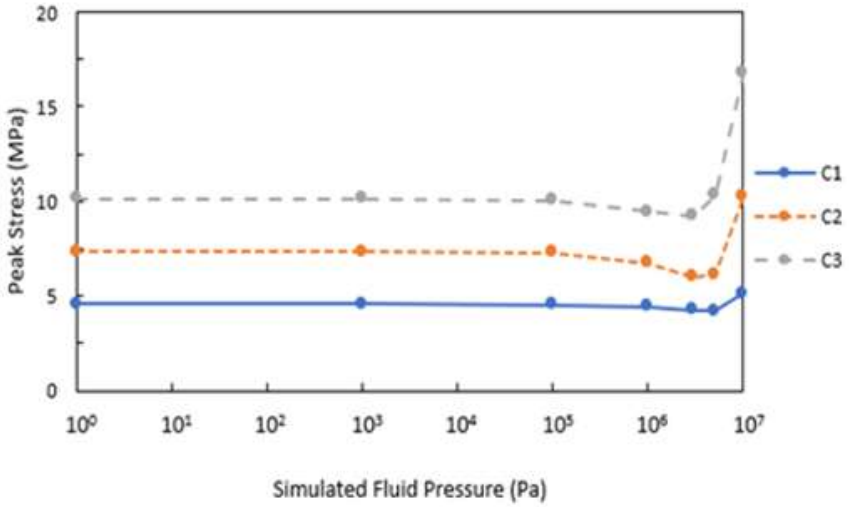

Figure 3.3. (A) Peak tensile stresses for bone. (B) Peak shear stresses for bone vs. simulated internal cyst fluid pressure (applied normal pressures). Tension values were the average of the top 1% of positive first principal stresses. Shear values were the average of the top 1% of maximum shear stresses.

Compressive stress magnitude decreased approximately 30% with 10 MPa normal pressure for cyst sizes C2 and C3, but it increased approximately 2% with 10 MPa normal pressure for cyst size C1 (Table 3.2). Tension had the largest relative change between normal pressures of 100 kPa to 5 MPa compared to shear and compression for cyst sizes C2 and C3. However, tensile stresses had the lowest baseline magnitude (less than 5 MPa). Thus, cyst

pressure did not increase the likelihood of bone damage and/or cyst growth until cyst pressures were above 5 MPa.

Table 3.2. Changes in Peak Stress Relative to Peak Stresses at 100 kPa Normal Pressure

Cyst size 1 (C1)	1 MPa	3 MPa	5 MPa	10 MPa
Compression	1% decrease	4% decrease	6% increase	2% increase
Tension	3% decrease	4% decrease	1% increase	27% increase
Shear	2% decrease	6% decrease	8% decrease	12% increase
Cyst size 2 (C2)				
Compression	7% decrease	23% decrease	34% decrease	29% decrease
Tension	17% increase	90% increase	188% increase	476% increase
Shear	7% decrease	17% decrease	16% decrease	41% increase
Cyst size 3 (C3)				
Compression	6% decrease	17% decrease	24% decrease	30% decrease
Tension	17% increase	83% increase	178% increase	488% increase
Shear	6% decrease	8% decrease	3% increase	67% increase

The filled-cyst models indicated possible levels of detrimental pressure in the cysts during joint compression. For all the models, the pressure on the cyst surface within the filled-cyst models was non-uniform, contrary to the assumption in the parametric normal pressure study (Figure 3.4). The approximate percent area of each cyst lining with pressures above 5 MPa was 6% (C1), 3% (C2), and 8% (C3). Pressures were at or below 5 MPa in the typical regions of cyst growth, on the sides and top of the cyst, for C2 and C3. Pressures did approach 10 MPa in the dome of the C1 small cyst and near the opening of the C3 large cyst.

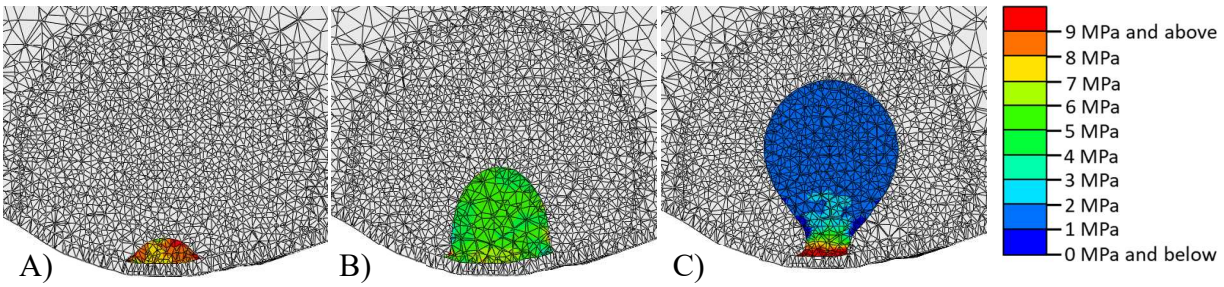

Figure 3.4. Pressure within cyst filling viewed from a para-sagittal section of the distal medial femoral condyle for (A) C1 Cyst, (B) C2 Cyst, and (C) C3 Cyst. Pressures along the edge of the cyst filling illustrate interface pressures on the cyst cavity walls.

Shear stress and tensile stress patterns showed considerable variation between filled-cyst models and models without filling or applied normal pressures for C1 and C2 (Figures 3.5 and 3.6). Shear and tension patterns were qualitatively similar in the C3 models. The magnitude of tensile stress in the C3 models showed a substantially larger area of high stress in the filled-cyst model compared to a model with no filling or applied normal pressures. The highest tensile stresses for all models was consistently at or near the cartilage defect. For tension, nearly all bone stresses were under 5 MPa, well under the yield stress. For the models without a cyst filling or applied normal pressures, most shear stresses were also well under the yield stress except near the opening of the filled C3 cyst. Bone shear stresses in all of the filled-cyst models were at or above 10 MPa near the cyst opening.

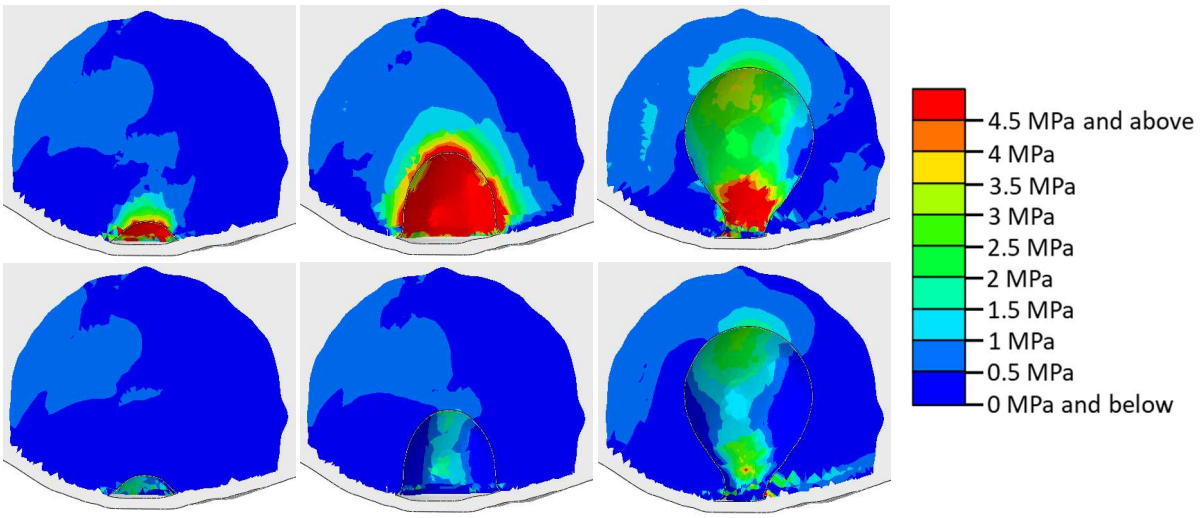

Figure 3.5. Top row: Tensile bone stress in the ROI and cyst walls viewed from a para-sagittal section of the distal medial femoral condyle for filled cyst models C1, C2, and C3. Bottom row: Bone tensile stresses for models with no applied pressure or cyst filling for C1, C2, and C3.

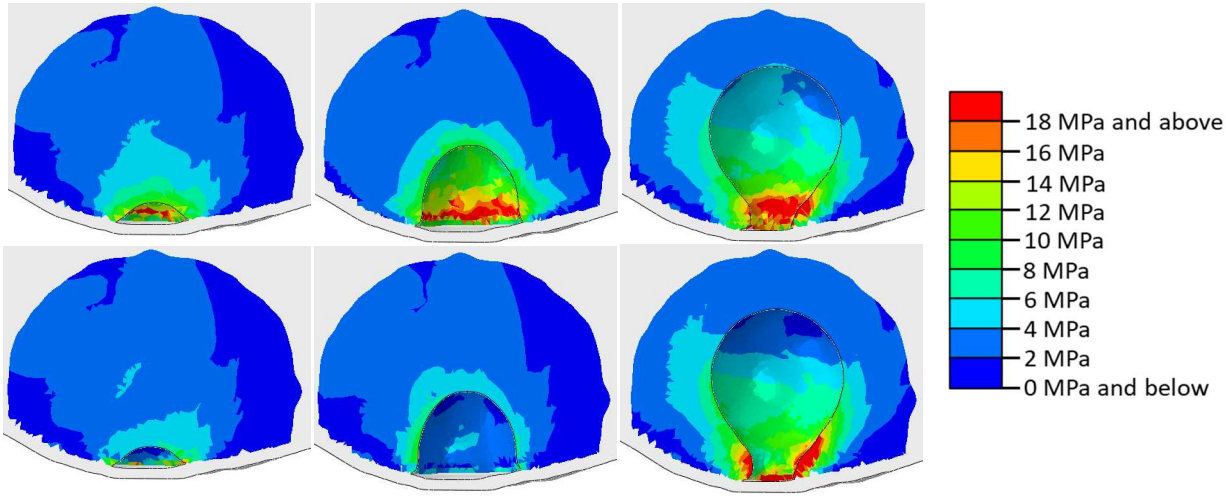

Figure 3.6. Top row: Bone shear stresses in the ROI and cyst walls viewed from a para-sagittal section of the distal medial femoral condyle for filled cyst models C1, C2, and C3. Bottom row: Bone shear stresses for empty cyst models with no applied pressure or cyst filling for C1, C2, and C3.

3.5 Discussion

This study indicates that compressive stresses generally decreased as cyst wall normal pressures increased. Changes in compressive stresses for the C1 cyst were smaller than those for

the C2 and C3 cysts. Tension had the largest relative change with increasing cyst pressure, and this is most likely due to smaller baseline values which never approached the bone yield strength. Approximate compressive yield strength for trabecular bone can be deduced from a combination of the work from Sanyal et al [26] and assuming a bone volume fraction range of 0.4-0.5 for trabecular bone [27]. This produces an estimated compressive yield strength range of 35-52 MPa and tensile yield strength range of 28-42 MPa (approximately 80% of the compressive yield strength). The work of Sanyal et al [26] and assuming a bone volume fraction range of 0.4-0.5 can also be used to estimate the shear yield strength range. This results in an estimate of 13-20 MPa for shear. Our results show baseline shear stresses for the medium(C2) and large(C3) cysts at the loads applied are only about 75% of the lower estimated yield stress. This supports prior work which predicts that shear stresses in the equine medial femoral condyle can approach failure stress and are likely the cause of cyst initiation and enlargement [8, 15]. Therefore, shear stresses appear to be the most important consideration for cyst growth. Since loads on the stifle joint during gallop are at least approximately three times greater than our current applied load [28], we predict shear stresses would exceed yield stress and drive cyst growth without any contributions from fluid pressure.

A combination of the parametric normal pressure model results and the filled-cyst model results can provide additional insights into influences on SBC growth and shape. The parametric normal pressure portion of the study indicates that cyst pressures need to be above 5 MPa to increase the likelihood of bone damage. However, the filled-cyst portion shows that pressures around that magnitude do not occur in areas of typical cyst growth. This suggests a mechanism for cyst growth other than fluid pressure (Figure 3.6). There is a tendency for the articular aspect of the cyst to become smaller as they mature (compare the shape of C2 and C3). For the filled-

cyst models, pressures in the cyst filling reached 10 MPa at the articular surface (opening) of the largest cyst studied (Figure 3.4). For the filled-cyst models, shear stresses approached yield at the opening near the articular surface (Figure 3.6). It may be that the elevated shear stresses at this location, perhaps in conjunction with high cyst fluid pressures, may be the explanation for why cysts do not fully close and heal.

Overall, this research indicates that intra-cyst fluid may contribute to the elevation of shear stresses in small- and medium-sized cysts to the point that shear yield strength is approached, but this does not occur in areas of expected cyst growth. When considering our conclusions about the effect of pressure in the cyst, several model characteristics must be considered. In regard to the parametric portion of our study, the data shows that larger cysts have higher baseline bone stresses. These models inherently possess a larger surface area for fluid pressure to act upon. Consequently, this may produce greater bone stresses. A noticeable trend in the data from parametric portion is the dip in shear stresses at applied pressures greater than 1 MPa and smaller than 10 MPa. This may be due to support for the bone provided by the applied pressures. This support may reduce the deformation of the bone and thus reduce shear, but extremely large applies pressures may then eliminate any supportive role and induce higher shear stresses in the bone. A difficult question is what level of cyst fluid pressure is likely to actually occur. A prior study by Bonilla et al. found that peak contact pressures in a stifle with an osteochondral defect reached approximately 2.5 MPa for an 1800 N load [29]. Thus, for a gallop load of approximately 8000 N, peak contact pressures could possibly reach 8-10 MPa. This study, with a resultant force of 3000 N, found peak contact pressure of about 6 MPa. When this is translated to gallop, it is clear peak contact pressures of 8-10 MPa could occur. However, the peak contact pressure would not likely translate directly to cyst fluid pressure of the same

magnitude because peak pressure would be confined to an extremely small region. In vivo cyst pressures must be nearly the same over the entire cyst surface for comparisons with our results. Thus, even an estimation of 5 MPa cyst pressure may be higher than actual cyst fluid pressures during gallop or less strenuous exercise.

Another consideration, with regard to our results, is the use of a continuum model with a simple solid cyst surface on which the pressure acts. Our model assumes solid surfaces on the interior of the cyst which leads to higher transfer of the cyst pressure to bone stress in our continuum model. When fluid pressure is applied inside a real cyst, it acts upon the porous trabecular bone network, soft tissue, and marrow in the bone network. Thus, the actual tissue level bone stresses may not be elevated as much as our model predicts by fluid pressure. An alternative approach would be to use fluid-structure interaction models, but this would markedly increase the complexity of the models and require assumptions about fluid properties and behavior governing flow. Fluid-structure interaction models would have been more appropriate if we expected substantial fluid flow, but the situation of interest is more focused on fluid pressurization. Our dual-simulation approach allows reasonable complexity of the model while providing insights into bone stresses surrounding the cyst with fluid pressurization.

The material modeled inside of the cyst was a soft solid based on the bulk modulus of water and an assumed high Poisson's ratio, so it was not a fluid. Soft solids have previously been used to simulate the contents within SBCs in the equine stifle joint and knee [8, 9] and the mandible [30]. The work of Frazer et al. [8] and McErlain et al. [9] focused on the mechanical trauma theory by investigating the mechanical effects of SBCs on the bone and surrounding joint. Frazer et al. [8] assumed a Young's modulus of 1 MPa for the cyst contents to reflect the absence of trabecular structure and likely presence of fibrous and fluid contents. McErlain et al.

[9] assumed a Young's modulus of 1e-6 MPa for the cyst contents after a pilot study where values from 1e-6 MPa to 30 MPa were computationally tested. They found no significant differences in stress values for elements surrounding the SBC, so they chose the lowest modulus value from their pilot study. Their finding has additional value in the context of our study and provides some additional support for our results. Sarrafpour et al. [30] assumed a Young's modulus of 0.1 MPa by reasoning that most radicular cysts contents resemble a hydrogel. Water and its properties have been previously used in place of synovial fluid within simulations of joint mechanics [31]. Synovial fluid, and other fluids which are likely to be present in the cyst, should flow relatively freely and perhaps would produce a more uniform pressure than seen our filled-cyst models. However, as previously mentioned, the additional complexities necessary for a fluid-structure interaction model that includes synovial fluid flow may not provide much additional insight beyond our results.

The impact of fluid pressure on SBC enlargement has had limited prior study. The only study the authors found in the literature was published by Cox et al. [14] who used a 2D model of trabecular bone to test the effects of fluid pressure on cyst growth. They used a similar method as the present study to model fluid pressure through a normal force on the cyst walls, and they reported that fluid pressure, osteocyte death, and a combination of the two increased cyst growth. Those authors note that the magnitude of the applied loads in their model are not critical because the underlying model mathematics scale them to produce a realistic bone turnover rate and structure parameters. However, the magnitude of applied loads and stresses is clearly an important factor. Thus, the study essentially assumes *a priori* that cyst growth will occur due to osteocyte death and/or fluid pressures. It did not consider other factors, such as tissue damage due to bone stresses. Our results show the importance of direct mechanical bone stresses and

indicate a possible limited contribution of fluid pressure for small and medium cysts as fluid pressure increases. Additionally, our results show that while it may be possible for fluid pressure to increase the stresses which may cause cyst growth, the necessary fluid pressures are not likely to occur in bone cysts in vivo.

We performed an analysis of simulated fluid pressure in three different SBC sizes through simulations of intra-cyst fluid and the use of different applied pressures on the inner cyst wall. We found that bone shear stresses (the most critical) did not appreciably increase until cyst pressures were over 5 MPa. In addition, for higher loading (such as gallop) and associated baseline bone stresses, even higher fluid pressures may be required to alter bone stresses. When considering the actual cyst fluid pressures likely to occur and the possible overestimation of the cyst pressure effect in our continuum model of trabecular bone, we conclude that cyst fluid pressure is unlikely to affect the growth of bone cysts.

3.6 References

1. Audrey, H.X., H.R. Abd Razak, and T.H. Andrew, The truth behind subchondral cysts in osteoarthritis of the knee. Open Orthop J, 2014. 8: p. 7-10.

2. Ghahremani, S., et al., *Osteochondral lesions in pediatric and adolescent patients.* Semin Musculoskelet Radiol, 2014. **18**(5): p. 505-12.

3. Tanamas, S.K., et al., *The association between subchondral bone cysts and tibial cartilage volume and risk of joint replacement in people with knee osteoarthritis: a longitudinal study.* Arthritis Res Ther, 2010. **12**(2): p. R58.

4. Frisbie, D.D., M.W. Cross, and C.W. McIlwraith, *A comparative study of articular cartilage thickness in the stifle of animal species used in human pre-clinical studies compared to articular cartilage thickness in the human knee.* Vet Comp Orthop Traumatol, 2006. **19**(3): p. 142-6.

5. Jeffcott, L.B., S.E. Kold, and F. Melsen, *Aspects of the pathology of stifle bone cysts in the horse.* Equine Vet J, 1983. **15**(4): p. 304-11.

6. Ray, C.S., et al., *Development of subchondral cystic lesions after articular cartilage and subchondral bone damage in young horses.* Equine Vet J, 1996. **28**(3): p. 225-232.

7. Verschooten, F. and A. De Moor, *Subchondral cystic and related lesions affecting the equine pedal bone and stifle.* Equine Vet J, 1982. **14**(1): p. 47-54.

8. Frazer, L.L., E.M. Santschi, and K.J. Fischer, *The impact of subchondral bone cysts on local bone stresses in the medial femoral condyle of the equine stifle joint.* Med Eng Phys, 2017. **48**: p. 158-167.

9. McErlain, D.D., et al., *Subchondral cysts create increased intra-osseous stress in early knee OA: A finite element analysis using simulated lesions.* Bone, 2011. **48**(3): p. 639-46.

10. Shirazi, R. and A. Shirazi-Adl, *Computational biomechanics of articular cartilage of human knee joint: effect of osteochondral defects.* J Biomech, 2009. **42**(15): p. 2458-65.

11. Landells, J.W., *The bone cysts of osteoarthritis.* J Bone Joint Surg Br, 1953. **35-b**(4): p. 643-9.

12. Reilingh, M.L., et al., *Morphological analysis of subchondral talar cysts on microCT.* Knee Surg Sports Traumatol Arthrosc, 2013. **21**(6): p. 1409-17.

13. Kold, S.E., J. Hickman, and F. Melsen, *An experimental study of the healing process of equine chondral and osteochondral defects.* Equine Vet J, 1986. **18**(1): p. 18-24.

14. Cox, L.G., et al., *The role of pressurized fluid in subchondral bone cyst growth.* Bone, 2011. **49**(4): p. 762-8.

15. Frazer, L.L., E.M. Santschi, and K.J. Fischer, *Impact of a void in the equine medial femoral condyle on bone stresses and peak contact pressures in a finite element model.* Vet Surg, 2019. **48**(2): p. 237-246.

16. Brommer, H., et al., *Functional adaptation of articular cartilage from birth to maturity under the influence of loading: a biomechanical analysis.* Equine Vet J, 2005. **37**(2): p. 148-54.

17. Carter, D.R. and W.C. Hayes, *The compressive behavior of bone as a two-phase porous structure.* J Bone Joint Surg Am, 1977. **59**(7): p. 954-62.

18. Diamant, I., R. Shahar, and A. Gefen, *How to select the elastic modulus for cancellous bone in patient-specific continuum models of the spine.* Med Biol Eng Comput, 2005. **43**(4): p. 465-72.

19. Mah, P., T.E. Reeves, and W.D. McDavid, *Deriving Hounsfield units using grey levels in cone beam computed tomography.* Dentomaxillofac Radiol, 2010. **39**(6): p. 323-35.

20. Hodgskinson, R. and J. Currey, *Young's modulus, density and material properties in cancellous bone over a large density range.* Journal of Materials Science: Materials in Medicine, 1992. **3**(5): p. 377-381.

21. Nazemi, S.M., et al., *Optimizing finite element predictions of local subchondral bone structural stiffness using neural network-derived density-modulus relationships for proximal tibial subchondral cortical and trabecular bone.* Clin Biomech (Bristol, Avon), 2017. **41**: p. 1-8.

22. Laasanen, M.S., et al., *Biomechanical properties of knee articular cartilage.* Biorheology, 2003. **40**(1-3): p. 133-40.

23. Butler, D.L., M.D. Kay, and D.C. Stouffer, *Comparison of material properties in fascicle-bone units from human patellar tendon and knee ligaments.* J Biomech, 1986. **19**(6): p. 425-32.

24. Donahue, T.L., et al., *A finite element model of the human knee joint for the study of tibio-femoral contact.* J Biomech Eng, 2002. **124**(3): p. 273-80.

25. Tissakht, M. and A.M. Ahmed, *Tensile stress-strain characteristics of the human meniscal material.* J Biomech, 1995. **28**(4): p. 411-22.

26. Sanyal, A., et al., *Shear strength behavior of human trabecular bone.* J Biomech, 2012. **45**(15): p. 2513-9.

27. Chevrier, A., et al., *Interspecies comparison of subchondral bone properties important for cartilage repair.* J Orthop Res, 2015. **33**(1): p. 63-70.

28. Robin, D., et al., *Ground reaction forces in the horse at the walk, trot and gallop measured with an instrumented shoe.* Computer Methods in Biomechanics and Biomedical Engineering, 2008. **11**(S1): p. 195-196.

29. Bonilla, A.G., et al., *Ex vivo equine medial tibial plateau contact pressure with an intact medial femoral condyle, with a medial femoral condylar defect, and after placement of a transcondylar screw through the condylar defect.* Vet Surg, 2015. **44**(3): p. 289-96.

30. Sarrafpour, B., et al., *Roles of functional strain and capsule compression on mandibular cyst expansion and cortication.* Arch Oral Biol, 2019. **98**: p. 1-8.

31. Hamid, K.S., et al., *The Role of Fluid Dynamics in Distributing Ankle Stresses in Anatomic and Injured States.* Foot Ankle Int, 2016. **37**(12): p. 1343-1349.

4. Design of a Modular MRI-Compatible Micropipette Simulator Towards Understanding How Design Affects Basilar Thumb Joint Contact Mechanics

Manuscript submitted to the Journal of Medical Devices

Running Title: MRI-Compatible Micropipette Simulator Design

Nolan M. Norton[A], MS

Kenneth J. Fischer[A,B,C], PhD

[A]The University of Kansas, Bioengineering Program

[B]The University of Kansas Medical Center, Orthopedics and Sports Medicine

[C]The University of Kansas, Mechanical Engineering

This research was supported by the University of Kansas General Research Fund Grant

Imaging services were provided by the Hoglund Biomedical Imaging Center and the University of Kansas Medical Center

Ethical approval was granted by the Human Subjects Committee Internal Review Board at the University of Kansas Medical Center

The corresponding author is Dr. Fischer

4.1 Abstract

Many laboratory technicians and researchers who frequently use micropipettes experience hand and upper limb disorders. The basilar thumb joint, also known as the first carpometacarpal or trapeziometacarpal joint, is commonly affected by osteoarthritis (OA). Mechanical factors are associated with OA initiation and progression. This study developed a MRI-compatible modular micropipette simulator that can be used to understand how micropipette design affects basilar thumb joint contact mechanics. A micropipette simulator with a cylindrical handle (length 127 mm, diameter 25 mm) was used with one subject to demonstrate the system's feasibility. Contact areas and pressures were similar to previously published data of basilar thumb joint models in power grasp and lateral pinch. The micropipette simulator addresses several limitations of current techniques for studying pipetting and provides insight into basilar thumb joint contact mechanics. It's modularity will allow future studies to examine handle design parameters such as handle diameter, cross-sectional shape, and other features.

Key Words: micropipette, design, finite element analysis

4.2 Introduction

The basilar thumb joint, also known as the trapeziometacarpal joint or the carpometacarpal joint, is one of the hand joints most affected by osteoarthritis (OA). It has been reported as the second most common joint for OA in the hand [1, 2] and OA of the joint is much more common in women than in men [1-3]. Actions that require repetitive squeezing or grasping have been casually linked to musculoskeletal problems in the hand and upper body. Pipetting within a medical laboratory or general research setting is one such daily task that has been linked to musculoskeletal complaints and problems in the upper extremities. Björksten et al reported a median yearly pipetting time of 313 hours in Swedish female lab technicians, and those that pipetted more than 300 hours per year carried higher risk towards developing hand and shoulder ailments [4]. David and Buckle reported that individuals who continuously pipette for periods longer than 30 minutes had a significantly greater chance of reporting hand complaints and that individuals who pipette more than 220 hours annually are more likely to report hand complaints [5]. Holm et al surveyed approximately 1200 female lab technicians and reported that pipetting was more closely associated with complaints than other lab tasks and that symptoms were greatest in the thumb and wrist for high weekly exposure to pipetting (> 5 hours) [6]. Experimental and computational methods have sought to examine the effects of pipetting. Experimental studies have mostly sought to understand how pipette design affects the hand and forearm through surveys/questionnaires, measurement of joint angles, and EMGs [4-16]. This information can be useful, but their results can be limited in their scope and these methods are susceptible to unavoidable issues such as personal bias in surveys and muscle signal crosstalk when collecting EMG data. Computational models have also been used to predict joint angles, muscle forces, and tendon displacements during pipetting [17-21]. However, these types of

models require several assumptions that include relying on generalized geometries and musculature. Therefore, they may not fully capture muscle activation patterns and forces, and they do not provide an insight into stresses that occur within the joints in question.

Contact and cartilage mechanics are critical towards assessing potential OA development and progression. Mechanical damage from repeated contact is believed to contribute to internal physical and biochemical changes in articular cartilage that lead to OA initiation and progression. Magnetic resonance imaging (MRI) based finite element analysis (FEA) is a recent technique that can be used to examine *in vivo* contact patterns and pressures within the basilar thumb joint during different functional activities such as pipetting. Additionally, MRI-based FEA allows for the minimization of boundary condition assumptions and the use of subject-specific geometries instead of generalized geometries. Specialized simulators are necessary for MRI-based FEA of functional activities. For safety reasons and to ensure image quality, ferromagnetic and other metallic materials should be avoided. We have constructed a modular plastic micropipette simulator that is compatible with MRI as well as computed tomography (CT) scanners. This system will allow researchers to analyze how different pipette features affect joint forces, contact area, and contact pressure distributions in the basilar thumb joint.

4.3 Methods

4.3.1 System Design

MRI-compatibility, modularity, and the reproducibility of experimental conditions were primary objectives for the design of the micropipette simulator. Ferromagnetic substances could not be included due to safety concerns, and other metals were excluded to avoid image distortion. Therefore, plastic materials were most appropriate, and additive manufacturing allowed straightforward fabrication of the parts and multiple versions to be tested.

Reproducibility of experimental conditions requires high sensitivity for the sensor and low friction (resistance) in moving parts so we can assure that the research participants are applying a consistent force. Modularity was required so different designs could be quickly and easily interchanged during human subjects testing.

To achieve modularity, the micropipette simulator was divided into multiple parts: a button to be pushed by the thumb, a carbon fiber plunger/rod to transfer button force through a handle, an O-ring on the far end of the rod to prevent the rod and button from falling out of the handle, and a two-piece spherical base that housed a pneumatic rubber bulb when it was fully assembled (Figure 4.1A). The two parts of the spherical base were fastened together using plastic nuts and bolts. Each handle set, with a button and push-rod, had internal female threads so it could be screwed onto the spherical base with male threads (Figure 4.1B).

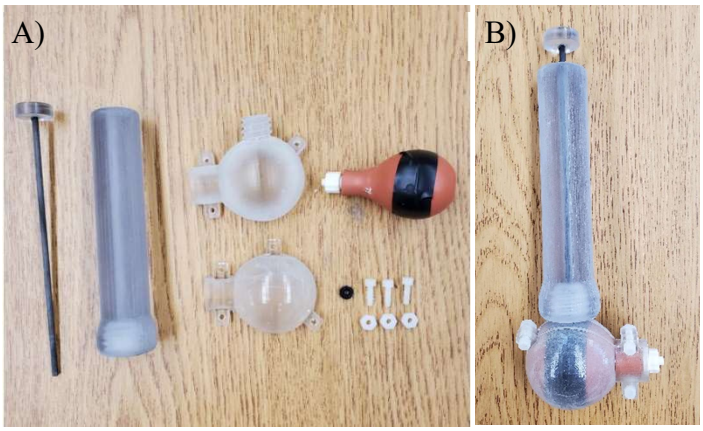

Figure 4.1. (A) Disassembled pipette simulator. (B) Assembled pipette simulator.

The rubber bulb was attached via plastic connectors and plastic tubing to a pneumatic system with two pressure regulators to assure a consistent pre-pressure of 1.0 psi before the micropipette plunger was pushed. The system also contained a precision pressure transducer to provide data and feedback to the subject during data collection (Figure 4.2). A personal computer was used to read and monitor the pressure transducer data. A custom LabVIEW code provided visual

feedback to the subject and allowed them to attain and hold the pressure at or near a specified target during the MRI scan. This system provided consistent resistance to plunger depression with minimal friction and a pressure precision of 0.001 psi. Early experiments with plastic and glass syringe designs had substantial friction which increased the force to move the piston from a static position and decreased force to hold the syringe pressure at a fixed level. This behavior of syringes was apparent even with lubricants. A micropipette with a cylindrical handle (handle length = 127 mm, handle diameter = 25 mm) was constructed for an initial test with one subject (Figure 4.1). To assure consistent and stable wrist position, the subject wore a MRI-compatible wrist brace, with approximately 20º wrist extension, during the simulated pipetting MRI scan.

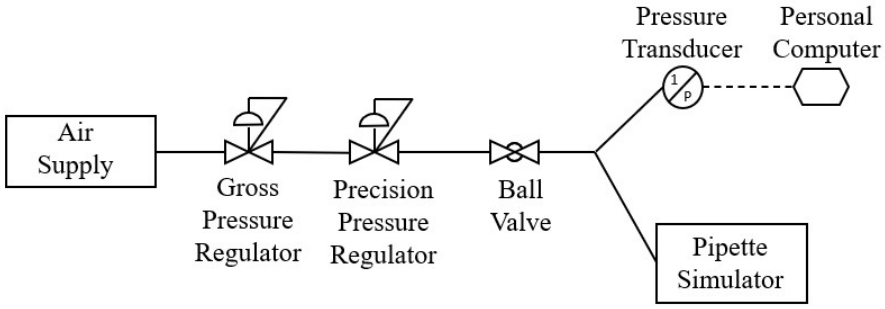

Figure 4.2. Simple instrumentation diagram for the pneumatic system.

4.3.2 Subject Recruitment and Imaging Protocol

One male subject (age = 28 years old) with no prior history of musculoskeletal disease participated in this study. Research protocols and consent forms were approved by the governing Institutional Review Board. MRI was acquired using a dual echo steady state (DESS) sequence in a 3T clinical scanner (Siemens Skyra). Two types of image sets were acquired for the subject. Images were acquired during simulated pipetting using the micropipette handle design described in section 4.3.1. The simulated pipetting images were collected at reduced resolution (in-plane voxel 0.31 mm by 0.31 mm and out-of-plane thickness 1.0 mm) with a scan time of 188

seconds. The wrist and thumb ray were also imaged while relaxed at high resolution (in-plane voxels 0.22 mm by 0.20 mm and out-of-plane thickness 0.5 mm) with a scan time of 4.5 minutes. Simulated pipetting involved pushing a plunger with the thumb, and consistent force was maintained through the use of the pneumatic system with the precision pressure transducer and visual feedback to the subject. A target pressure of 1.125 psi was determined by trial and error to create minimal fatigue and discomfort and allow the subject to hold the pipetting force and position for up to four minutes. Reduced scan times also helped to minimize subject fatigue and related motion artifacts.

4.3.3 Finite Element Model Definition

MR images for both the loaded and unloaded configuration were manually segmented using ScanIP 7.1 to isolate the metacarpal and trapezium. Their respective articular cartilage was also segmented for only the unloaded configuration. ScanIP was used to generate tetrahedra finite element meshes of the bones and cartilage from the unloaded image set. FEBio Studio was used to define and execute a displacement-driven FEA model. Displacement boundary conditions for the FEA were defined in a similar manner to previously published studies that utilized MRI-based modeling [22-24]. Briefly, kinematic transformations to align the loaded and unloaded configurations were defined using 3D voxel-based image registration of the metacarpal. Image registration was also used to determine the translations and rotations (transformation) that placed the unloaded trapezium into its loaded position and orientation (i.e. the kinematics for the FEA). Before solving the FEA model, the trapezium was translated away from the metacarpal to remove contact at the start of the simulation. During the process of solving the FEM, the trapezium was translated back to the final position with contact. Deformation of the subchondral bone was assumed to be negligible during a light-loading task

such as the pipetting simulation, so the metacarpal and trapezium were modeled as rigid bodies. Articular cartilage was assumed to behave as a Neo-hookean material with an effective (relaxation) modulus of 1.0 MPa [25, 26] and a Poisson's ratio of 0.20 due to the length of the scan in the loaded configuration [27-29]. Contact area, contact force magnitude, and elemental contact pressure were tracked during the simulation and were directly available from FEBio Studio. The model results from the metacarpal articular surface were collected and visualized using the FEBio software suite. A Custom MATLAB code was written to sort the raw contact pressure data and calculate the average of the top 1% of contact pressure values, which will be reported as peak pressure.

4.4 Results

For the single trial subject, the contact area was 16 mm^2, the contact force was 1.5 Newtons, and the peak contact pressure was 0.3 MPa. The contact on the metacarpal surface was volar and medial (Figure 4.3).

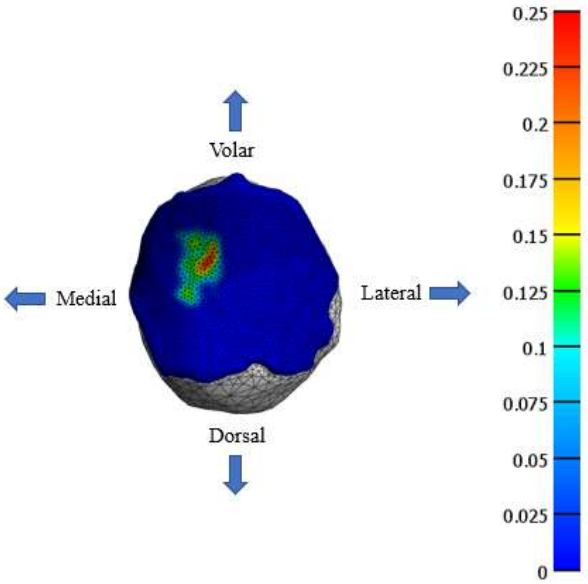

Figure 4.3. Contact pressure distribution (magnitude in MPa) for the basilar thumb joint model.

Contact measures were compared to previously published computational studies which examined contact mechanics in the basilar thumb joint during power grasp and lateral pinch by Dourthe et al [30] and Schneider et al [31] (Figure 4.4). Measurements for contact area and peak contact pressure from our pipetting model were of a similar magnitude to reported values from power grasp and lateral pinch.

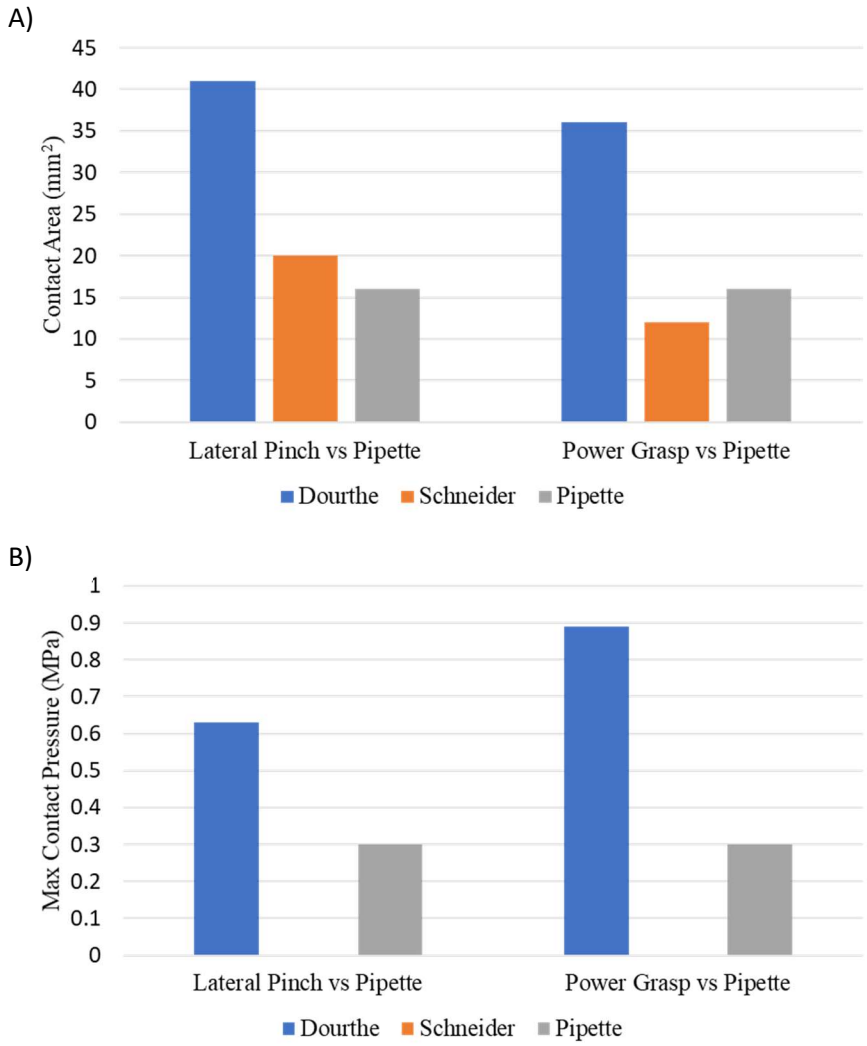

Figure 4.4. Comparison of contact measures between the pipetting model and models for power grasp and lateral pinch for (A) contact area and (B) peak contact pressure.

A sensitivity analysis was run for Poisson's ratio ranging from 0.05-0.45 (Appendix A.2). The results indicated that the model was relatively insensitive to changes in Poisson's ratio below 0.3. A Poisson's ratio above 0.3 would not be appropriate for our models given the subject's long-term loading.

4.5 Discussion

MRI-based FEA is a method that can be used to analyze in vivo contact measures within the basilar thumb joint during functional activities that experimental and other computational methodologies cannot provide. Experimental studies mainly rely on kinematic data that is collected using markers placed on the skin, EMG data collected using sensors placed on the skin, asking study participants to subjectively assess specific pipette designs, or some combination of these. These methodologies have several positive aspects. Familiarity has been shown to affect how users perceive different pipettes [11], and experimental studies can provide insight into users' thoughts and preferences on different design parameters which affect comfort during pipette usage. They are also non-invasive and do not require the length of time that is necessary to define subject-specific FEA model geometries and boundary conditions. Methodologies utilizing kinematic or EMG data can provide descriptions of what occurs around the basilar thumb joint and, in some cases, estimate forces applied to the joint. However, they are unable to analyze contact area or contact pressure distribution within the joint. This is important in understanding how cartilage is loaded because it may become damaged due to repeated loading. Additionally, significant limitations exist for purely kinematic studies and user feedback methodologies that can influence the collected data and results. The hand contains several muscles within a confined anatomical space that allow for precise control. EMG sensors are carefully placed on the surface to analyze contractions of specific muscles, but it is likely that

sensors pick up crosstalk from neighboring muscles without an ability to separate the contributions of each perceived muscle. The crosstalk complicates any conclusions that can be drawn about specific muscle activity. Needle electrodes can be used, but they are less well tolerated and may not capture/characterize activity in the entire muscle. Additionally, while linear relationships between EMG data amplitude and muscle force have been used, the relationship between EMG data amplitude and muscle force can be non-linear [32]. Therefore, only general conclusions can be drawn about the effects of observed muscular activity on joints in the hand and wrist. In regard to kinematic data, motion markers placed on the skin can experience significant skin motion artifacts which makes it difficult to capture accurate bone rotations and displacements [33]. Conversely, MRI-based FEA does not rely on recording muscular activity or optimal marker kinematic data to analyze the joint. The process used to define model boundary conditions can account for the complexity of muscular contractions necessary for micropipette usage. In addition to addressing limitations of other experimental methods, MRI-based FEA provides overall advantages and additional data.

Computational models have been used to supplement experimental studies to gain further understanding of how pipetting affects the hand. There are several positive aspects of currently published models. They provide an analysis of multiple joints in the thumb, and they provide an analysis of several factors such as joint angles, muscle forces, constraint forces, and tendon displacements. However, they are not without some limitations. Currently published models rely on generalized bone geometries, generalized musculature geometries and attachments, and kinematic data as a model input. MRI-based FEA has the advantages of using subject-specific models while also not depending on the definition of musculature geometries and force-driven inputs throughout the loading cycle. The process to determine inputs for the displacement-driven

model only depends on the initial state of the bones during relaxation and their final state during loading. Wu et al noted that the variability in how subjects accomplish a given task caused large standard deviations in both predicted joint and muscles forces [19]. Notably, they also observed that predicted tendon displacement was not largely affected by variability in subject behavior [20]. This highlights that some types of data, such as joint angles, may not be able to provide insights beyond the assessed subjects; other types of data, such as tendon displacement, are less sensitive to subject variations and could provide insights that are applicable beyond the assessed subjects. Larger scale MRI-based FEA studies of pipette design may provide insights into how various pipette design parameters affect the basilar thumb joint mechanics.

Measurement of contact mechanics during pipetting via MRI-based modeling is experimentally challenging, so comparisons to published literature concerning the basilar thumb joint help to verify and validate our modeling approach (Figure 4.4). The breadth of published finite element models, or related mathematical models, that focus on the basilar thumb joint is limited. Given the further limited amount of literature concerning contact mechanics during pipetting, comparisons to similar activities are necessary. Pipetting has been described as a combination of power and precision grasp, so comparisons to reported results of power grasp are reasonable. The orientation of the thumb during lateral pinch and pipetting is similar, so comparisons to computational lateral pinch data are also useful. Dourthe et al used finite deformation biphasic theory with mathematical modeling to examine contact pressure and area during lateral pinch and power grasp [30]. They reported an average contact area of 36 mm^2 and an average maximum (peak) contact pressure of 0.89 MPa on the metacarpal articular surface for power grasp, and they reported an average contact area of 41 mm^2 and an average maximum contact pressure of 0.63 MPa on the metacarpal articular surface for lateral pinch [30]. Schneider

et al used a finite element model in FEBio to examine contact area during several functional activities [31]. They reported a trapezial contact area of 12 mm^2 for men and 13 mm^2 for women during power grasp, and they reported a trapezial contact area of 21 mm^2 for men and 20 mm^2 for women during lateral pinch [31]. Our contact area is in the range of those reported. Our peak pressure was lower than those studies reported, but the force in the simulator is relatively low. Both Dourthe et al and Schneider et al reported lateral contact on the articular surface during power grasp; Dourthe et al reported central-volar contact during lateral pinch whereas Schneider et al reported central contact during lateral pinch. Our results indicated somewhat central-volar contact. This may be explained by differences between power grasp and pipetting and by subject variability. Comparisons to power grasp and lateral pinch data can provide an expected magnitude of contact measures, but exact pressures and locations cannot be directly compared due to differences in the orientation of the thumb and lower force in our study. Schneider et al also modeled the articular cartilage as a Neo-Hookean solid, but they chose a Young's modulus of 10 MPa for the cartilage. Notably, their choice was not based on reported modulus results for the basilar thumb joint. Our model utilized a Young's modulus of 1 MPa, and that was based on published studies analyzing articular cartilage within the basilar thumb joint [25, 26].

A key feature of our micropipette simulator is that its modularity enables interchanging of the micropipette handle. Different handles can be quickly designed and printed to isolate or combine design parameters such as handle diameter, handle shape, and inclusion of a finger rest. Our experiment utilized MRIs to prevent subject exposure to radiation and provide clearer visualization of soft tissues, but this system could also operate with CT and other imaging modalities. When comparing our results to other published data, some limitations of the proposed micropipette simulator should be noted. The length of the scan in the loaded

configuration limits the target load and lowers the magnitude of the contact measures. A small pressure for plunger resistance was used to minimize fatigue and motion artifact, and the thumb tip force provided by the chosen simulator pressure has not yet been compared to the thumb tip force that a typical micropipette would require during aspiration or while dispensing liquid. This might partially explain why our contact measurements were smaller than the reported values for grasp. Regardless, the simulator can be used to compare forces and contact pressures for various design features without the need for specific target values of thumb tip force. The magnitude of our simulated contact mechanics are similar to previously published work which provides confidence that the described micropipette simulation technique can produce reliable results. Future studies can also compare area measured directly from then loaded MRI scans to the FEA model contact area as a means of model verification.

We developed an adaptable micropipette simulator that is modular, compatible with MRI and other imaging modalities, and could be used in experimental studies. This system addresses many of the current limitations of experimental and other computational methods used to study micropipette design. The micropipette simulator, along with MRI-based modeling, will contribute to micropipette design research by enabling an analysis of how micropipette design features affect contact mechanics in the basilar thumb joint.

4.6 References

1. Dahaghin, S., et al., *Prevalence and pattern of radiographic hand osteoarthritis and association with pain and disability (the Rotterdam study).* Ann Rheum Dis, 2005. **64**(5): p. 682-7.

2. Wilder, F.V., J.P. Barrett, and E.J. Farina, *Joint-specific prevalence of osteoarthritis of the hand.* Osteoarthritis Cartilage, 2006. **14**(9): p. 953-7.

3. Zhang, Y., et al., *Prevalence of symptomatic hand osteoarthritis and its impact on functional status among the elderly: The Framingham Study.* Am J Epidemiol, 2002. **156**(11): p. 1021-7.

4. Björksten, M.G., B. Almby, and E.S. Jansson, *Hand and shoulder ailments among laboratory technicians using modern plunger-operated pipettes.* Appl Ergon, 1994. **25**(2): p. 88-94.

5. David, G. and P. Buckle, *A questionnaire survey of the ergonomie problems associated with pipettes and their usage with specific reference to work-related upper limb disorders.* Applied Ergonomics, 1997. **28**(4): p. 257-262.

6. Holm, J.W., O.S. Mortensen, and F. Gyntelberg, *Upper limb disorders among biomedical laboratory workers using pipettes.* Cogent Medicine, 2016. **3**(1): p. 1256849.

7. Asundi, K.R., J.M. Bach, and D.M. Rempel, *Thumb force and muscle loads are influenced by the design of a mechanical pipette and by pipetting tasks.* Hum Factors, 2005. **47**(1): p. 67-76.

8. Fredriksson, K., *Laboratory work with automatic pipettes: a study on how pipetting affects the thumb.* Ergonomics, 1995. **38**(5): p. 1067-73.

9. Kim, E., F. Aqlan, and A. Freivalds, *Development of an ergonomic four-finger-push manual pipette design.* Appl Ergon, 2020. **85**: p. 103045.

10. Lee, Y.H. and M.S. Jiang, *An ergonomic design and performance evaluation of pipettes.* Appl Ergon, 1999. **30**(6): p. 487-93.

11. Lichty, M.G., I.L. Janowitz, and D.M. Rempel, *Ergonomic evaluation of ten single-channel pipettes.* Work, 2011. **39**(2): p. 177-85.

12. Maija, L. and N. Nina, *Ergonomics and the usability of mechanical single-channel liquid dosage pipettes.* International Journal of Industrial Ergonomics, 2006. **36**(3): p. 257-263.

13. Ming-Lun, L., et al., *An investigation of hand forces and postures for using selected mechanical pipettes.* International Journal of Industrial Ergonomics, 2008. **38**(1): p. 18-29.

14. Park, J.K. and B. Buchholz, *Effects of work surface height on muscle activity and posture of the upper extremity during simulated pipetting.* Ergonomics, 2013. **56**(7): p. 1147-58.

15. Rempel, P., et al., *The effect of two alternative arm supports on shoulder and upper back muscle loading during pipetting.* Work, 2011. **39**(2): p. 195-200.

16. Sormunen, E. and N. Nevala, *User-oriented evaluation of mechanical single-channel axial pipettes.* Appl Ergon, 2013. **44**(5): p. 785-91.

17. Kim, E. and A. Freivalds, *Two-dimensional biomechanical thumb model for pipetting.* International Journal of Industrial Ergonomics, 2018. **68**: p. 165-175.

18. Wu, J.Z., et al., *Inverse dynamic analysis of the biomechanics of the thumb while pipetting: a case study.* Med Eng Phys, 2012. **34**(6): p. 693-701.

19. Wu, J.Z., et al., *Analysis of the musculoskeletal loading of the thumb during pipetting--a pilot study.* J Biomech, 2014. **47**(2): p. 392-9.

20. Wu, J.Z., et al., *The musculoskeletal loading profile of the thumb during pipetting based on tendon displacement.* Med Eng Phys, 2013. **35**(12): p. 1801-10.

21. Wu, J.Z., et al., *Analysis of the Constraint Joint Loading in the Thumb During Pipetting.* J Biomech Eng, 2015. **137**(8): p. 084501.

22. Johnson, J.E., et al., *Computationally efficient magnetic resonance imaging based surface contact modeling as a tool to evaluate joint injuries and outcomes of surgical interventions compared to finite element modeling.* J Biomech Eng, 2014. **136**(4): p. 0410021-9.

23. Modaresi, S., et al., *Evaluation of midcarpal capitate contact mechanics in normal, injured and post-operative wrists.* Clin Biomech (Bristol, Avon), 2017. **47**: p. 96-102.

24. Pillai, R.R., et al., *MRI-based modeling for evaluation of in vivo contact mechanics in the human wrist during active light grasp.* J Biomech, 2007. **40**(12): p. 2781-7.

25. Dourthe, B., et al., *Assessment of healthy trapeziometacarpal cartilage properties using indentation testing and contrast-enhanced computed tomography.* Clinical Biomechanics, 2019. **61**: p. 181-189.

26. Rivers, P.A., et al., *Osteoarthritic changes in the biochemical composition of thumb carpometacarpal joint cartilage and correlation with biomechanical properties.* J Hand Surg Am, 2000. **25**(5): p. 889-98.

27. Boschetti, F., et al., *Biomechanical properties of human articular cartilage under compressive loads.* Biorheology, 2004. **41**: p. 159-166.

28. Jurvelin, J.S., M.D. Buschmann, and E.B. Hunziker, *Optical and mechanical determination of Poisson's ratio of adult bovine humeral articular cartilage.* J Biomech, 1997. **30**(3): p. 235-41.

29. Korhonen, R.K., et al., *Comparison of the equilibrium response of articular cartilage in unconfined compression, confined compression and indentation.* J Biomech, 2002. **35**(7): p. 903-9.

30. Dourthe, B., et al., *In vivo contact biomechanics in the trapeziometacarpal joint using finite deformation biphasic theory and mathematical modelling.* Med Eng Phys, 2016. **38**(2): p. 108-14.

31. Schneider, M.T.Y., et al., *Trapeziometacarpal joint contact varies between men and women during three isometric functional tasks.* Med Eng Phys, 2017. **50**: p. 43-49.

32. Staudenmann, D., et al., *Methodological aspects of SEMG recordings for force estimation--a tutorial and review.* J Electromyogr Kinesiol, 2010. **20**(3): p. 375-87.

33. Fuller, J., et al., *A comparison of lower-extremity skeletal kinematics measured using skin- and pin-mounted markers.* Human movement science, 1997. **16**(2-3): p. 219-242.

5. Effects of Micropipette Handle Diameter and Inclusion of Finger Rest on Basilar Thumb Joint Contact Mechanics

Manuscript submitted to Medical Engineering and Physics

Running Title: Effects of Micropipette Handle and Finger Rest

Nolan M. Norton[A], MS

Kenneth J. Fischer[A,B,C], PhD

[A]The University of Kansas, Bioengineering Program

[B]The University of Kansas Medical Center, Orthopedics and Sports Medicine

[C]The University of Kansas, Mechanical Engineering

This research was supported by the University of Kansas General Research Fund Grant

Imaging services were provided by the Hoglund Biomedical Imaging Center and the University of Kansas Medical Center

Ethical approval was granted by the Human Subjects Committee Internal Review Board at the University of Kansas Medical Center

The corresponding author is Dr. Fischer

5.1 Abstract

Micropipette users commonly experience problems in the hand and upper limbs. Mechanical factors are thought to contribute to osteoarthritis (OA) initiation and progression in the basilar thumb joint. Finite element analysis can be used to examine the effects of micropipette design on contact mechanics measures within the basilar thumb joint. This pilot study examined the effect of micropipette handle diameter (12 mm, 25 mm, and 40 mm) and the presence of a finger rest on contact area, contact force, and peak contact pressure in the basilar thumb joint. All contact mechanics measures decreased with increasing handle diameter with significant differences between the 12 mm diameter and the 40 mm diameter handles. Decreasing contact mechanics measures with increasing diameter confirmed our hypothesis. Contact mechanics measures were higher ($p < 0.05$) with a finger rest for contact area and force. We expected contact measures to decrease with the presence of a finger rest. The unexpected outcome may have been due to non-randomized testing order and fatigue during testing.

Key words: micropipette, design parameters, joint mechanics, ergonomics, finite element analysis

5.2 Introduction

The basilar thumb joint, also known as the trapeziometacarpal joint or the carpometacarpal joint, is the second most likely joint in the hand to be affected by osteoarthritis (OA) [1, 2]. OA in the basilar thumb joint is three times more likely in women than in men [1-3]. Pipetting within a laboratory or general research setting, as well as other tasks that require repetitive squeezing or grasping, has been casually linked to musculoskeletal complaints and problems in the upper extremities. Björksten et al reported a median yearly pipetting time of 313 hours in Swedish female lab technicians, and those that pipetted more than 300 hours per year carried higher risk towards developing hand and shoulder ailments [4]. David and Buckle reported that individuals who continuously pipette for periods longer than 30 minutes had a significantly greater chance of reporting hand complaints and that individuals who pipette more than 220 hours annually are more likely to report hand complaints [5]. Holm et al surveyed approximately 1200 female lab technicians and reported that pipetting was more closely associated with complaints than other lab tasks and that symptoms were greatest in the thumb and wrist for high weekly exposure to pipetting (> 5 hours) [6]. Experimental methods have sought to examine the effects of micropipette design through surveys/questionnaires, measurement of joint angles, estimation of muscle forces, and EMGs [4-16]. Experimental studies that have used these methods have examined either one commercially available design or compared multiple commercially available designs. This information can be useful for direct comparisons of the used micropipettes or the effects of a particular design, but otherwise their results can be limited in their scope. Current computational studies have utilized one micropipette design during their analysis of joint angles, muscle forces, and tendon

displacements during pipetting [17-21]. This provides data and conclusions about each particular micropipette design, but these conclusions about micropipette design cannot be generalized.

Current and past micropipette designs are an amalgamation of design parameters such as handle cross-sectional size, handle shape, and supportive features such as a finger rest. An investigation into the effects of specific micropipette design factors on OA-susceptible joints could establish a foundation of knowledge and influence future designs with an aim towards reducing stress in the basilar thumb joint and hand. Systematic analysis techniques are necessary to isolate and investigate the effects of specific micropipette design parameters on OA-susceptible joints such as the basilar thumb joint. A modular plastic micropipette simulator used with MRI-based finite element analysis (FEA) was previously developed to allow this pilot study. Additive manufacturing (3D printing) with plastic material was used for the creation of different simulator handles to isolate specific micropipette design features. An investigation into the impact of basic features of handle diameter and finger rest inclusion was performed to provide a foundation that can be used to assess future directions of micropipette design analysis. Our first hypothesis was that increasing the micropipette handle diameter would decrease contact area, contact force, and peak contact pressures in the basilar thumb joint. Our second hypothesis was that the presence of a finger rest would decrease contact area, contact force, and peak contact pressure.

5.3 Methods

5.3.1 Micropipette Simulator Designs

The modular micropipette simulator consisted of a button to be pushed by the thumb, a carbon fiber plunger/rod to transfer button force through a handle, an o-ring on the far end of the rod to prevent the rod and button from falling out of the handle, and a two-piece spherical base

that houses a pneumatic rubber bulb when it was fully assembled (Figure 5.1A). The two parts of the spherical base were fastened together using plastic nuts and bolts. Each handle set, with a button and push-rod, had internal female threads so it could be screwed onto the spherical base with male threads (Figure 5.1B). The rubber bulb was attached via plastic connectors and tubing to a pneumatic system with two pressure regulators to assure a consistent pre-pressure of 1.0 psi before the micropipette plunger was pushed. The system also contained a precision pressure transducer to provide data and feedback to the subject during data collection. A personal computer was used to monitor the pressure transducer data and send visual feedback to the subject during the MRI scan. This system provided consistent resistance to plunger depression with minimal friction and a pressure precision of 0.001 psi. A custom LabVIEW code provided visual feedback to the investigators and allowed the subjects to attain and hold the pressure at or near a specified target during the MRI scan.

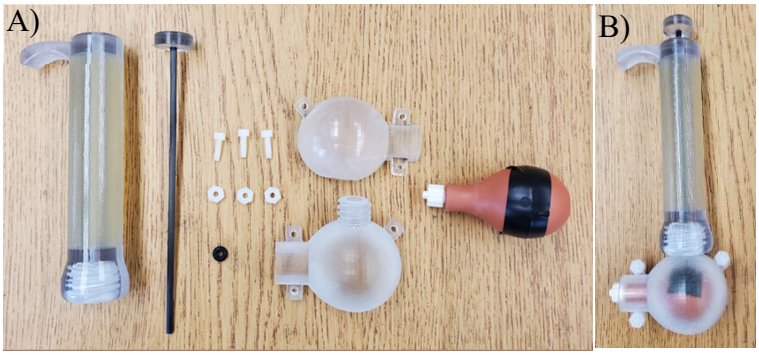

Figure 5.1. (A) Disassembled pipette simulator of 25 mm handle diameter with a finger rest. (B) Assembled pipette simulator.

All the handles were variations of a cylinder without any cross-sectional shape adjustments. A combination of three diameters (12 mm, 25 mm, and 40 mm) and the inclusion or exclusion of a finger rest produced six micropipette handles (Figure 5.2). All the handles had a length of 127 mm. Additionally, each subject wore a MRI-compatible wrist brace with

approximately 20º wrist extension to assure consistent and stable wrist position throughout the duration of the scan with the micropipette.

Figure 5.2. Micropipette handles with varying diameter and finger rest presence. From left to right: 40 mm diameter with and without a finger rest, 25 mm diameter with and without a finger rest, 12 mm diameter with and without a finger rest.

5.3.2 Subject Recruitment and Imaging Protocol

Three male subjects (average age = 30 years, range 28-33) and two female subjects (average age = 27.5 years, range 27-28) with no prior history of musculoskeletal disease participated in this pilot study. Research protocols and consent forms used for informed consent were approved by the governing Institutional Review Board. MRIs were acquired using a dual echo steady state (DESS) sequence in a 3T clinical scanner (Siemens Skyra). Two types of image sets were acquired for each subject. The wrist and thumb ray were imaged while relaxed at high resolution (in-plane voxels 0.22 mm by 0.20 mm and out-of-plane thickness 0.5 mm) with a scan time of 4.5 minutes. Images were also acquired during simulated pipetting using the micropipette handles described in section 5.3.1. Reduced scan times also helped to minimize subject fatigue and motion artifacts. The simulated pipetting images were collected at reduced resolution (in-plane voxel 0.31 mm by 0.31 mm and out-of-plane thickness 1.0 mm) with a scan time of 188 seconds. Simulated pipetting involved pushing a plunger with the thumb, and consistent force was maintained through the use of the pneumatic system with the precision pressure transducer and visual feedback to the subject. A target pressure of 1.125 psi was determined by trial and

error to create minimal fatigue and discomfort and allow the subject to hold the pipetting force and position for up to four minutes. Because of concerns about fatigue over the course of testing, the test order was not randomized, so it was set to test the expectedly more difficult handles in each of two groups first with a 10 minute rest period between groups. First, the micropipette handles (12 mm, 25 mm and 40 mm) without a finger rest were tested. Next, the scan to acquire the unloaded image set was completed to provide the subject a substantial rest break. Finally, the micropipette handles with a finger rest were tested. Within each set of handles, diameters were tested from smallest (presumed most difficult) to largest (presumed easiest).

5.3.3 Finite Element Model Definition and Statistical Analysis

MR images for both the loaded and unloaded configuration were manually segmented using ScanIP 7.1 to isolate the metacarpal and trapezium. Their respective articular cartilage was also segmented for only the unloaded configuration. ScanIP was also used to generate tetrahedra finite element meshes of the bone and cartilage from the unloaded image set. FEBio Studio was used to define and execute displacement-driven finite element models (FEMs). Boundary conditions for the displacement-driven FEMs were defined in a similar manner to previously published studies that utilized MRI-based modeling [22-24]. Briefly, kinematic transformations to align the loaded and unloaded configurations were defined using 3D voxel-based image registration of the metacarpal. The image registration was also used to define the translations and rotations that placed the unloaded trapezium into a loaded position (i.e. the kinematics for the FEM). Before the FEM was solved, the trapezium was translated away from the metacarpal to remove contact at the start of the simulation. During the process of solving the FEM, the trapezium was translated back to the loaded position with contact. Deformation of the subchondral bone was assumed to be negligible during a light-loading task such as the

micropipette simulation, so the metacarpal and trapezium were modeled as rigid bodies. Articular cartilage was assumed to behave as a Neo-hookean material with an effective relaxation modulus of 1.0 MPa [25, 26] and a Poisson's ratio of 0.20 due to the length of the scan in the loaded configuration [27-29]. Contact area, contact force, and contact pressure were tracked during the simulation. Contact area, contact force magnitude, and elemental contact pressure data were directly available from FEBio Studio. A Custom MATLAB code was written to sort the raw contact pressure data and calculate the average of the top 1% of values which was reported as peak pressure. Mesh convergence was analyzed using elements with target edge lengths of 1.0 mm, 0.5 mm, and 0.25 mm. The results were consistent when changing the target edge length by half, so the finest resolution mesh was used for theoretical accuracy.

5.3.4 Statistical Analysis

A custom R code was written to perform a two-way repeated-measures multivariate analysis of variance (MANOVA) and subsequent one-way repeated-measures analysis of variance (ANOVA) and paired t-tests to determine statistical differences between the six handle designs. Before statistical analyses were completed, the data was examined to confirm if it met the necessary assumptions for repeated measures MANOVA and ANOVA. The assumptions for repeated-measures MANOVA include no univariate or multivariate outliers, multivariate normality of residuals (which can be approximately assessed by examining univariate normality of residuals for all independent variables), no multicollinearity, and sphericity. Visual examination of the data, the Shapiro-Wilks test, and Q-Q plots were used to assess for outliers and check normality. The Pearson correlation coefficient was used to assess multicollinearity. Mauchly's test was used to check sphericity. Statistical significance was set at $p < 0.05$.

5.4 Results

5.4.1 Statistical Analysis Assumptions

Data for one female subject could not be processed due to the MR image quality, which was poor for all images due to apparent motion artifact. Data for the remaining subjects was analyzed. The contact area, force and peak pressure data were plotted to assess potential multivariate (Figure 5.3) and univariate outliers (Figure 5.4). Multicollinearity, as assessed by Pearson correlation, was found to exist between contact area and contact force ($r = 0.91$, $p < 0.001$), contact area and peak contact pressure ($r = 0.88$, $p < 0.001$), and contact force and peak contact pressure ($r = 0.91$, $p < 0.001$). High correlations between dependent variables, such as those observed in our data, are highly problematic for repeated-measures MANOVA. Therefore, we could not perform that type of analysis.

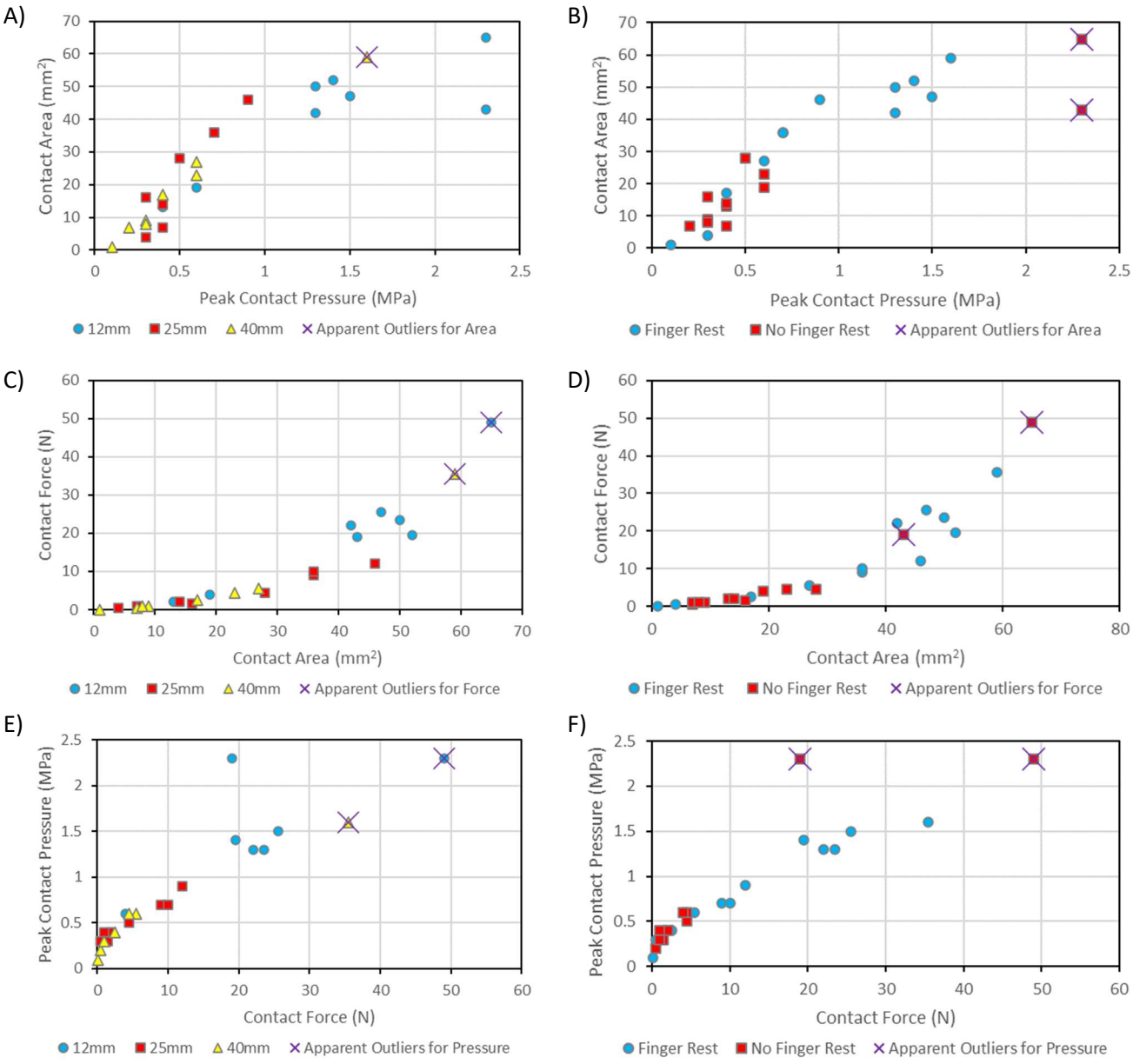

Figure 5.3. (A-B) plots of contact area against peak contact pressure for varying diameter and presence of finger rest. (C-D) plots of contact force against contact area for varying diameter and presence of finger rest. (E-F) plots of peak contact pressure against contact force for varying diameter and presence of finger rest. Apparent multivariate outliers for the measure on the y-axis are marked on each plot.

Univariate residual normality for diameter and contact area ($p = 0.3$), diameter and contact force ($p = 0.055$), diameter and peak contact pressure ($p = 0.6$), finger rest and contact area ($p = 0.1$), finger rest and contact force ($p = 0.068$), and finger rest and peak contact pressure ($p = 0.5$) was confirmed using the Shapiro-Wilk test and examination of Q-Q plots (Appendix A.4). Mauchly's test for sphericity for each diameter-finger rest interaction and diameter factor was insignificant in each analysis, so sphericity was not violated. Other than some apparent outliers, the assumptions of repeated measures ANOVA were satisfied.

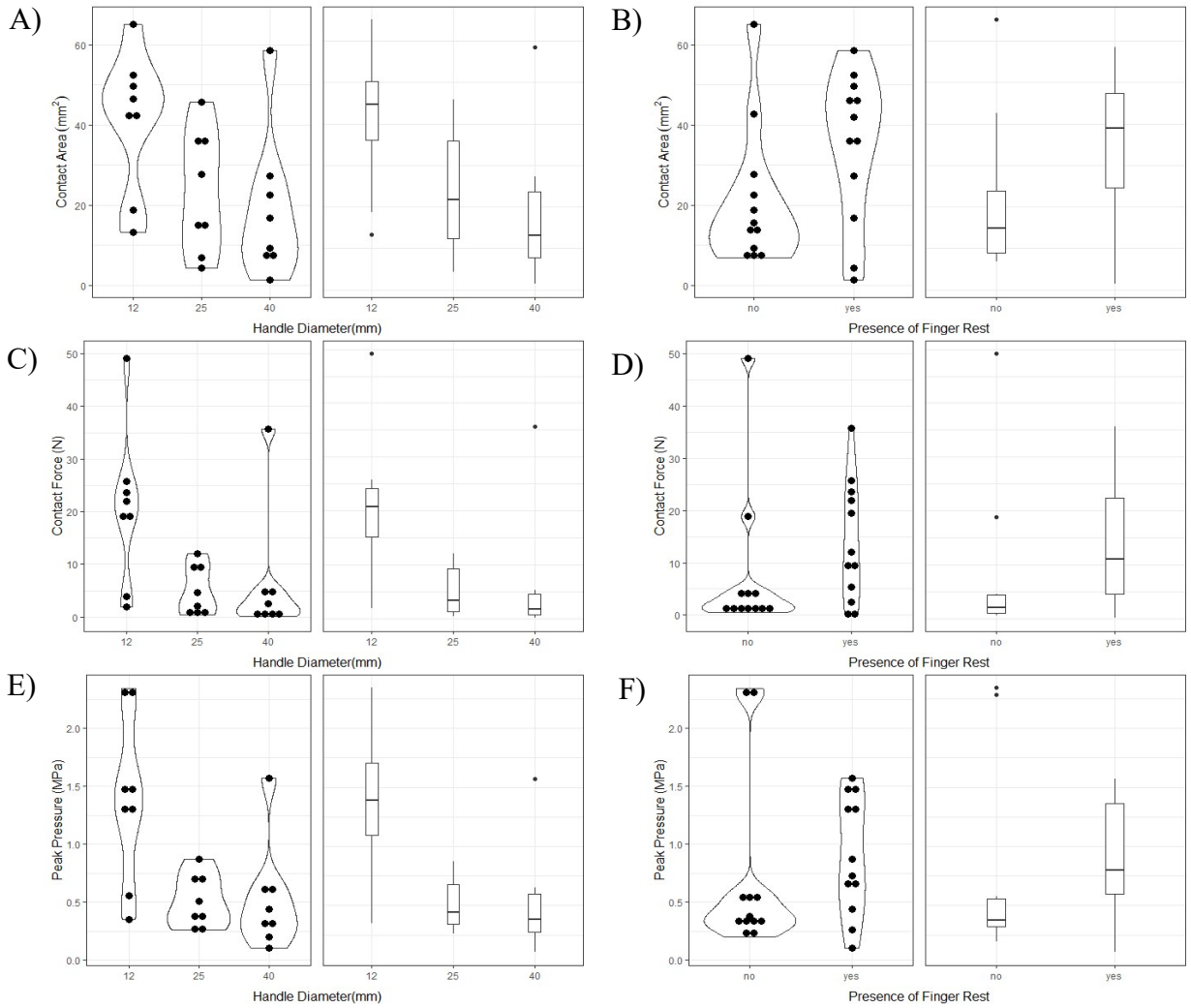

Figure 5.4. (A-B) violin and box plots of contact area for varying diameter and presence of finger rest. (C-D) violin and box plots of contact force for varying diameter and presence of finger rest. (E-F) violin and box plots of peak contact pressure for varying diameter and presence of finger rest.

5.4.2 Repeated Measures ANOVA Results

To account for the possible interaction of finger rest presence and handle diameter, two-way repeated measures ANOVA was used for each of the contact measures (Table 5.1).

Table 5.1. P-values for Two-Way Repeated Measures ANOVAs			
	Contact Area	Contact Force	Peak Contact Pressure
Diameter-Finger Rest Interaction	p = 0.9	p = 0.9	p = 0.8
Diameter	p = 0.01 ***	p = 0.01 ***	p = 0.004 ***
Finger Rest	p = 0.007 ***	p = 0.02 ***	p = 0.2

The interaction terms from the two-way repeated measures ANOVA were insignificant. Thus, we examined one-way repeated measures ANOVA with a Bonferroni post-hoc correction for the significant diameter factors from Table 5.1 (Table 5.2). The finger rest factor has only two levels, so no further tests were required for them.

Table 5.2. P-values for One-Way Repeated Measures ANOVAs for Diameter			
	Contact Area	Contact Force	Peak Contact Pressure
12mm – 25mm	p = 0.2	p = 0.2	p = 0.09
25mm – 40mm	p = 1.0	p = 1.0	p = 1.0
12mm – 40mm	p = 0.002 ***	p = 0.007 ***	p = 0.03 ***

5.4.3 Contact Pressure Location

Contact pressure was consistent within subjects (Appendix A.3). Finger Rest models showed larger contact pressures than No Finger Rest models for 12 mm diameter handles, and contact pressures decreased with increasing handle diameter (Figure 5.5).

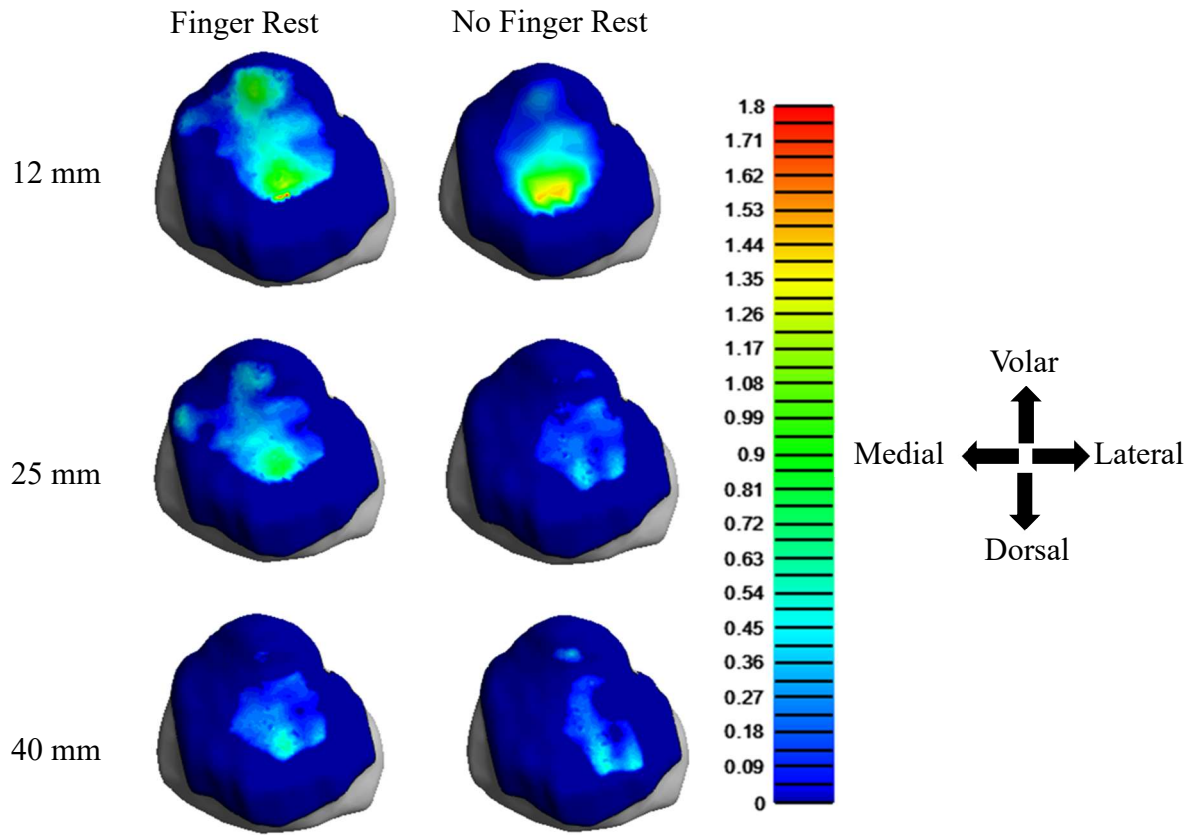

Figure 5.5. Contact pressure plots for one example subject. Contact pressure location was consistent across conditions. Contact pressure was the largest for the 12 mm diameter and decreased with increasing handle diameter.

5.5 Discussion

The effects of hand tool handle size and shape have been the focus of many research efforts. Experimental studies have reported that increasing cylindrical handle diameter decreased handle contact forces [30-32] and either increased contact area of the hand and fingers when assessing diameters from 30-48 mm [30] or decreased contact area of the hand and fingers when

assessing diameters from 51-83 mm [33]. Our micropipette study observed that articular surface contact force, contact area, and peak contact pressure all decreased with increasing handle diameter (max 40 mm). Significant differences for all contact measures were only observed between the 12 mm and 40 mm handle. However, qualitative analysis of the data distributions (Figures 5.3 & 5.4) indicates that noteworthy differences may exist between 12 mm and 25 mm handles. These results followed our expectations and provided a preliminary indication that larger diameter cylindrical micropipettes are more advantageous for repetitive work than smaller cylindrical micropipettes. However, our study produced the unexpected result that contact area, contact force, and peak contact pressure increased with the presence of a finger rest. Our expectation was that the finger rest would provide an additional source of stabilization, reduce the necessary grip strength and overall muscle tension, and thereby reduce contact mechanics measures. Our chosen non-randomized order of micropipette simulator tests could have contributed to this result through unrecognized fatigue. The finger rest designs were all tested after the relaxed anatomical scan which was intended to provide a substantial rest break. Fatigue could have increased stresses on the joint and therefore increase contact measures between articular surfaces through muscle coactivation. Some studies have been published on the effects of fatigue on muscle coactivation in the hand, wrist, and forearm [34-35]. These studies have reported some contradictory findings, but the different tasks used during data collection can make direct comparisons difficult. However, they have generally supported the conclusion that fatigue increases muscle coactivation. For example, Contessa et al reported increased activation of several forearm muscles in young subjects with fatigue of the first dorsal interosseous [34]. Another study, performed by Arellano et al, reported greater muscle coactivation of forearm muscles in older adults than younger adults while maintaining wrist extension or flexion [35].

Wrist position in our study was held constant across subjects. In addition to maintaing consistent conditions across subjects, this may have limited some effects of fatigue that would have been due to varying wrist position. Our chosen order was a result of uncertainty over how subjects would respond to the entire set of MRI tests with the simulator and a desire to put the handles perceived as most difficult first. This was to help assure we could collect a complete set of data for all designs and all subjects. Though it was unintended, the chosen order appears to have highlighted the effects of fatigue on model results. Future studies should randomize the order of micropipette designs and include longer rest breaks to reduce the possible effects of fatigue.

Several studies have sought to define optimal handle diameters that maximize grip force. Reported handle diameters for maximum grip force range from 33-40 mm [36, 37]. Maximizing grip strength can be useful for some tasks, but it could be detrimental for pipetting. Given the typical length of time workers use a micropipette, handle diameters that enable maximal grip force could exacerbate musculoskeletal pathologies if workers grip the handle more tightly as they fatigue. We did not directly measure handle contact force or grip force during data collection, but our results for the Finger Rest models suggest grip forces may increase with fatigue. An overall consideration for micropipette design should be user comfort. Studies of user comfort have generally reported a quadratic relationship between comfort and cylindrical handle diameter with a vertex between 30-40 mm [32, 38]. Micropipette users' familiarity with micropipette designs has also been shown to affect how they view them [11], so future endeavors could survey user comfort ratings to allow for comparisons between those ratings and contact measures for different handle diameters. Additional handle diameters between 25 mm and 40 mm and beyond 40 mm could be tested to further define the relationship between contact measures, handle diameter, and user comfort.

Our pilot study clearly has some limitations. One factor that could not be controlled is the grip force on the pipette. Increased grip force increases the contact force on the skin which, along with co-contractures of muscles within the hand, affects stresses on the joints within the hand. Increased grip force may have been used to stabilize the micropipette during later test runs. However, grip strength may not easily be controlled within our experimental procedure. Subjects were already focused on maintaining one pressure level, and adding another could markedly increase the difficulty. Another limitation is the lack of balance between male and female subjects. Men have reported greater grip strengths than women while using cylindrical handles [32, 39]. This could have skewed the data. Restrictions on human subjects protocols due to COVID-19 increased the difficulty recruiting subjects. Unfortunately, data from one female subject could not be analyzed due to MRI quality. In addition, the remaining data had previously noted univariate outliers. We included the univariate outliers in the analyses because they were the only violation of repeated measures ANOVA assumptions. Their inclusion would increase the standard deviations of the data, and thus decrease the power, but we still found significant differences within the data that match conclusions from visual assessment of the data. Future studies could work with a larger sample size to account for potential outliers to increase the power of the study and to allow analyses of differences between males and females. The process of manual segmentation, registration, and model definition and analysis requires a substantial amount of time. Financial resources and project timelines for a larger study would need to account for the investigator-intensive modeling process.

In conclusion, we found that increasing handle diameter decreased joint contact mechanics measures. This suggests that small cross section micropipettes should be avoided for long-duration, repetitive micropipetting tasks. This research also has numerous future directions.

Continued investigations into micropipette design that utilize FEA can provide unique insights into the effects of different design factors. Handle texture, hardness, weight, and shape are other potential factors that can be analyzed. Care must be taken while incorporating these design factors into experiments to account for subject fatigue.

5.6 References

1. Dahaghin, S., et al., *Prevalence and pattern of radiographic hand osteoarthritis and association with pain and disability (the Rotterdam study).* Ann Rheum Dis, 2005. **64**(5): p. 682-7.

2. Wilder, F.V., J.P. Barrett, and E.J. Farina, *Joint-specific prevalence of osteoarthritis of the hand.* Osteoarthritis Cartilage, 2006. **14**(9): p. 953-7.

3. Zhang, Y., et al., *Prevalence of symptomatic hand osteoarthritis and its impact on functional status among the elderly: The Framingham Study.* Am J Epidemiol, 2002. **156**(11): p. 1021-7.

4. Björksten, M.G., B. Almby, and E.S. Jansson, *Hand and shoulder ailments among laboratory technicians using modern plunger-operated pipettes.* Appl Ergon, 1994. **25**(2): p. 88-94.

5. David, G. and P. Buckle, *A questionnaire survey of the ergonomie problems associated with pipettes and their usage with specific reference to work-related upper limb disorders.* Applied Ergonomics, 1997. **28**(4): p. 257-262.

6. Holm, J.W., O.S. Mortensen, and F. Gyntelberg, *Upper limb disorders among biomedical laboratory workers using pipettes.* Cogent Medicine, 2016. **3**(1): p. 1256849.

7. Asundi, K.R., J.M. Bach, and D.M. Rempel, *Thumb force and muscle loads are influenced by the design of a mechanical pipette and by pipetting tasks.* Hum Factors, 2005. **47**(1): p. 67-76.

8. Fredriksson, K., *Laboratory work with automatic pipettes: a study on how pipetting affects the thumb.* Ergonomics, 1995. **38**(5): p. 1067-73.

9. Kim, E., F. Aqlan, and A. Freivalds, *Development of an ergonomic four-finger-push manual pipette design.* Appl Ergon, 2020. **85**: p. 103045.

10. Lee, Y.H. and M.S. Jiang, *An ergonomic design and performance evaluation of pipettes.* Appl Ergon, 1999. **30**(6): p. 487-93.

11. Lichty, M.G., I.L. Janowitz, and D.M. Rempel, *Ergonomic evaluation of ten single-channel pipettes.* Work, 2011. **39**(2): p. 177-85.

12. Maija, L. and N. Nina, *Ergonomics and the usability of mechanical single-channel liquid dosage pipettes.* International Journal of Industrial Ergonomics, 2006. **36**(3): p. 257-263.

13. Ming-Lun, L., et al., *An investigation of hand forces and postures for using selected mechanical pipettes.* International Journal of Industrial Ergonomics, 2008. **38**(1): p. 18-29.

14. Park, J.K. and B. Buchholz, *Effects of work surface height on muscle activity and posture of the upper extremity during simulated pipetting.* Ergonomics, 2013. **56**(7): p. 1147-58.

15. Rempel, P., et al., *The effect of two alternative arm supports on shoulder and upper back muscle loading during pipetting.* Work, 2011. **39**(2): p. 195-200.

16. Sormunen, E. and N. Nevala, *User-oriented evaluation of mechanical single-channel axial pipettes.* Appl Ergon, 2013. **44**(5): p. 785-91.

17. Kim, E. and A. Freivalds, *Two-dimensional biomechanical thumb model for pipetting.* International Journal of Industrial Ergonomics, 2018. **68**: p. 165-175.

18. Wu, J.Z., et al., *Inverse dynamic analysis of the biomechanics of the thumb while pipetting: a case study.* Med Eng Phys, 2012. **34**(6): p. 693-701.

19. Wu, J.Z., et al., *Analysis of the musculoskeletal loading of the thumb during pipetting--a pilot study.* J Biomech, 2014. **47**(2): p. 392-9.

20. Wu, J.Z., et al., *The musculoskeletal loading profile of the thumb during pipetting based on tendon displacement.* Med Eng Phys, 2013. **35**(12): p. 1801-10.

21. Wu, J.Z., et al., *Analysis of the Constraint Joint Loading in the Thumb During Pipetting.* J Biomech Eng, 2015. **137**(8): p. 084501.

22. Johnson, J.E., et al., *Computationally efficient magnetic resonance imaging based surface contact modeling as a tool to evaluate joint injuries and outcomes of surgical interventions compared to finite element modeling.* J Biomech Eng, 2014. **136**(4): p. 0410021-9.

23. Modaresi, S., et al., *Evaluation of midcarpal capitate contact mechanics in normal, injured and post-operative wrists.* Clin Biomech (Bristol, Avon), 2017. **47**: p. 96-102.

24. Pillai, R.R., et al., *MRI-based modeling for evaluation of in vivo contact mechanics in the human wrist during active light grasp.* J Biomech, 2007. **40**(12): p. 2781-7.

25. Dourthe, B., et al., *Assessment of healthy trapeziometacarpal cartilage properties using indentation testing and contrast-enhanced computed tomography.* Clinical Biomechanics, 2019. **61**: p. 181-189.

26. Rivers, P.A., et al., *Osteoarthritic changes in the biochemical composition of thumb carpometacarpal joint cartilage and correlation with biomechanical properties.* J Hand Surg Am, 2000. **25**(5): p. 889-98.

27. Boschetti, F., et al., *Biomechanical properties of human articular cartilage under compressive loads.* Biorheology, 2004. **41**: p. 159-166.

28. Jurvelin, J.S., M.D. Buschmann, and E.B. Hunziker, *Optical and mechanical determination of Poisson's ratio of adult bovine humeral articular cartilage.* J Biomech, 1997. **30**(3): p. 235-41.

29. Korhonen, R.K., et al., *Comparison of the equilibrium response of articular cartilage in unconfined compression, confined compression and indentation.* J Biomech, 2002. **35**(7): p. 903-9.

30. Welcome, D., et al., *An investigation on the relationship between grip, push and contact forces applied to a tool handle.* International Journal of Industrial Ergonomics, 2004. **34**(6): p. 507-518.

31. Aldien, Y., et al., *Contact pressure distribution at hand–handle interface: role of hand forces and handle size.* International Journal of Industrial Ergonomics, 2005. **35**(3): p. 267-286.

32. Kong, Y.-K. and B.D. Lowe, *Optimal cylindrical handle diameter for grip force tasks.* International Journal of Industrial Ergonomics, 2005. **35**(6): p. 495-507.

33. Seo, N.J. and T.J. Armstrong, *Investigation of grip force, normal force, contact area, hand size, and handle size for cylindrical handles.* Hum Factors, 2008. **50**(5): p. 734-44.

34. Contessa, P., et al., *Contribution from motor unit firing adaptations and muscle coactivation during fatigue.* J Neurophysiol, 2018. **119**(6): p. 2186-2193.

35. Arellano, C.J., et al., *Fatigue-induced adjustment in antagonist coactivation by old adults during a steadiness task.* J Appl Physiol (1985), 2016. **120**(9): p. 1039-46.

36. Sancho-Bru, J.L., et al., *Optimum tool handle diameter for a cylinder grip.* J Hand Ther, 2003. **16**(4): p. 337-42.

37. Thomas, W.M., et al., *Effects of handle size and shape on measured grip strength.* International Journal of Industrial Ergonomics, 2012. **42**(2): p. 199-205.

38. Yakou, T., et al., *Sensory evaluation of grip using cylindrical objects.* JSME International Journal Series C Mechanical Systems, Machine Elements and Manufacturing, 1997. **40**(4): p. 730-735.

39. Dong, R.G., et al., *A new approach to characterize grip force applied to a cylindrical handle.* Med Eng Phys, 2008. **30**(1): p. 20-33.

6. Conclusion

6.1 Summary

Finite element analysis enabled this examination of mechanics related to musculoskeletal diseases, such as osteoarthritis (OA) and the related subchondral bone cyst (SBC), in the equine stifle joint and the human basilar thumb joint. Specifically, fluid pressure was simulated within a SBC to examine its possible contributions to SBC growth. A plastic modular micropipette simulator was created to enable analyses of specific micropipette design features while using MRI-based finite element analysis (FEA). The effects of micropipette handle diameter and the presence of a finger rest on contact mechanics in the basilar thumb joint were examined.

6.2 Major Findings and Conclusions

6.2.1 Fluid Pressure Unlikely to Contribute to SBC Growth

Chapter 3 examined mechanics of the bone surrounding SBCs both with and without simulated fluid pressure. Fluid pressure was simulated through application of normal forces to the cyst wall or by placing a soft solid within the cyst. Models with applied normal forces showed that the magnitude of bone stresses did not substantially change until the resulting uniform simulated fluid pressure met or exceeded 5 MPa. Tension and compression in bone surrounding the cysts did not approach estimated yield strengths for any simulated fluid pressure. Shear stresses at small and moderate simulated fluid pressures were around estimated yield strengths for bone, and they increased with simulated fluid pressures greater than 5 MPa. Models with the soft solid filling showed that simulated fluid pressures which exceed 5 MPa are most likely to occur at the opening of cysts. This is not the area where typical cyst growth is expected, but it may explain why the cyst opening near the joint narrows but does not close as cyst size increases. These findings suggest that fluid pressure is not the dominant source of mechanical

trauma and does not noticeably contribute to mechanical trauma that drives cyst growth.

6.2.2 Benefits of Plastic Micropipette Simulator

Contact mechanics are important for understanding the development of OA within joints. Experimental studies of micropipettes are unable to provide insights into contact mechanics within the basilar thumb joint. Additionally, they have commonly used commercially available micropipettes that are a combination of various design choices. Non-invasive computational techniques, such as MRI-based FEA, can be used to investigate contact mechanics within the basilar thumb joint. Chapter 4 detailed the fabrication of a modular micropipette simulator for use with MRI-based FEA techniques. The components of the simulator included a handle, carbon fiber rod with a plastic button to transfer force through the handle, a two-piece spherical base, and a pneumatic rubber bulb. Additive manufacturing with a plastic resin was used to ensure MRI compatibility. Modularity was desired so that micropipette handles with different designs, which isolate different design features, could be easily exchanged throughout data collection. The pneumatic rubber bulb was connected to an adjustable pressure system which enabled reproducible experimental conditions. A LabVIEW program provided visual feedback to the subject concerning how much force they applied to the plastic button during the course of a MRI scan. One subject was scanned to demonstrate the viability of the technique. Contact area, contact force, and peak contact pressure were similar to values reported for lateral pinch and power grasp.

6.2.3 Effects of Micropipette Designs

Chapter 5 detailed a pilot study which utilized the aforementioned micropipette simulator to examine the effects of handle diameter and inclusion of a finger reset on contact mechanics within the basilar thumb joint. Displacement-driven finite element models were executed for four

subjects who each used three handle diameters (12 mm, 25 mm, and 40 mm) both with and without a finger rest. Contact area, contact force, and peak contact pressures were significantly smaller in the largest handle diameter (40 mm) when compared to the smallest (12 mm) handle diameter. This result confirmed our hypothesis regarding handle diameter. However, results concerning the presence of a finger rest did not confirm our hypothesis for that condition. Contact area and contact force were significantly larger for handles with a finger rest than those without a finger rest. This may have been influenced by the non-random order of handle evaluation during data collection. Overall, this pilot study demonstrated the ability of MRI-based FEA to examine differences in contact measures within the basilar thumb joint during pipetting.

6.3 Future Work

6.3.1 Models Using Human Data

The current study with the equine stifle joint, along with previous research into the contributions of mechanical trauma on subchondral bone, has provided foundational knowledge about SBC formation and growth. SBCs in the equine stifle commonly form in relatively young (yearling) horses, so the subchondral bone has not been impacted by OA. Bone material properties were estimated using CT Hounsfield units, so working with scans of bone that were assumedly unaffected by OA helped to isolate the effects of SBCs and factors that drive their growth. However, these studies cannot entirely explain the nature of SBCs within human knees. The equine stifle joint and human knee share several anatomical similarities, but differences exist between the two that are critical towards a more complete understanding of SBC occurrence in humans. SBCs are commonly noted as a cofactor of OA, so their surrounding bone is likely affected by OA in the early stages of development. This difference would be present in the bone material properties derived from human CT scans. An analysis of human SBC models, with this

study's results as a comparative baseline, could further elucidate the role of subchondral bone stresses in SBC formation and growth.

6.3.2 Utilize Micropipette Simulator in Experimental Studies

The micropipette simulator system was specifically designed for MRI-based FEA, but it is compatible with other imaging modalities. CT scans have been used in modeling studies of the hand, and they could provide some benefits over MRI. The necessary MRI scan duration can result in motion artifacts. The duration of CT scans is shorter than MRIs. However, subjects are exposed to some radiation over multiple scans, and soft tissues are not as visible on CT scans as they are on their MR images. Models which use CT images as a basis would require some assumptions of soft tissue shape and size which could impact model results. The shorter duration of CT scans would allow for greater pneumatic pressures that likely bear a closer resemblance to the resistance experienced while using commercial micropipettes. However, imaging protocols that maintain the viability of our approach for defining model boundary conditions would need to be considered. Comparative studies which use both MRI and CT data could provide insight into the cost and benefits of both approaches. Alternatively, a combination of the two imaging modalities could produce a method that utilizes the strengths of MR and CT images. MR images provide greater visualization of the articular cartilage than CT scans, so MRI scans of the unloaded state, a state without pipetting or performing any other functional activity, could be recorded for the creation of subject-specific geometries that do not rely on assumptions concerning cartilage shape. CT images provide a clearer boundary between the bones and their surroundings both visually and in terms of pixel greyscale values, so they could be utilized for the loaded scans to shorten the segmentation process. Articular cartilage is not isolated on the loaded scans, so the use of CT scans would not be a detriment to the process. Effectively

shortening the segmentation process is crucial for future studies on a larger scale. Segmentation is the most time-consuming step in the process, and the total time would be substantially greater with 10-15 or more subjects who each test multiple micropipette designs. Additionally, the use of CT scans for the loaded images could help combat issues of fatigue throughout testing through shorter scan times.

The modular micropipette system could also be used in experimental studies that focus on collecting different kinds of data focused on how pipetting affects the hand. Past research into the effects of pipetting have utilized commercially available micropipettes. This approach can limit the applicability of results to certain designs, and it does not fully address the fundamental questions of how specific micropipette design features affect users. The usage of the modular micropipette simulator with other types of studies can increase the understanding of how basic design parameters affect the hand and end users. Image-based modeling studies can provide unique insights within joints, but they can be time-intensive and require assumptions for material property inputs. Experimental studies such as questionnaires focusing on user preferences, kinematic studies, and muscle activation pattern studies are less time-consuming alternatives that can examine the effects of pipetting from different viewpoints. Questionnaires provide feedback on the thoughts of end users, and this data can be valuable for guiding new micropipette designs. Kinematic studies and muscle activation pattern studies provide a quicker turnaround than modeling studies. Kinematic studies can estimate forces and moments acting on joints and provide joint angle data for characterizing how pipette design affects movement of joints in the hand. Muscle activation pattern studies can be used to examine how micropipette design affects muscles in the hand and forearm. They can also be used to assess how muscles compensate for fatigue while pipetting.

6.3.3 Additional Design Variations of Micropipette

Handle diameter and presence of a finger rest are two of many parameters that can be tested with the micropipette simulator system. Handle texture, hardness, weight, and cross-sectional shape are a few parameters that could also be examined. The size of handles with a particular cross-sectional shape may compared to a user's hand dimensions. User comfort could also be surveyed for each handle to provide additional information for design assessment. Designs of different handles can be easily created in CAD software and fabricated by additive manufacturing. Care must be taken when outlining future studies to consider the type of statistical analyses used and their requirements. Additionly, the number and nature of designs tested should account for impact on subjects, particularly with respect to fatigue. The testing order should be randomized to account for the possible effect of fatigue. The use of CT scans to shorten the duration of scans while pipetting could allow for multiple tests to be performed with each pipette handle throughout the examination period.

Appendix

A.1 Mesh Quality Information and Evaluation Criterion for Equine Stifle Joint Models

Shape Factor: 0 = degenerate element, 1 = optimal element shape

Min Angle of Element: Should be greater than 5

Max Angle of Element: Should be less than 170

Aspect Ratio: Ratio between longest and shortest edge of element, should be less than 10

A.1.1 C1 (Element Set: NEWROI)

Number of Tet elements verified: 98382

Min angle on Tri Faces < 5: 0 (0%)

Average min angle on tri faces: 42.50, Worst min angle on tri faces: 13.91

Max angle on Tri faces > 170: 0 (0%)

Average max angle on tri faces: 83.29, Worst max angle on tri faces: 136.80

Aspect ratio > 10: 0 (0%)

Average aspect ratio: 1.49, Worst aspect ratio: 3.32

Shape factor < 0.0001: 0 (0%)

Average shape factor: 0.759783, Worst shape factor: 0.036502

Analysis errors: 0 (0%), Analysis warnings: 0 (0%)

A.1.2 C2 (Element Set: NEWROI)

Number of Tet elements verified: 92218

Min angle on Tri Faces < 5: 0 (0%)

Average min angle on tri faces: 42.20, Worst min angle on tri faces: 13.28

Max angle on Tri faces > 170: 0 (0%)

Average max angle on tri faces: 83.50, Worst max angle on tri faces: 134.94

Aspect ratio > 10: 0 (0%)

Average aspect ratio: 1.50, Worst aspect ratio: 4.42

Shape factor < 0.0001: 0 (0%)

Average shape factor: 0.755012, Worst shape factor: 0.036676

Analysis errors: 0 (0%), Analysis warnings: 0 (0%)

A.1.3 C3 (Element Set: NEWROI)

Number of Tet elements verified: 81538

Min angle on Tri Faces < 5: 0 (0%)

Average min angle on tri faces: 41.24, Worst min angle on tri faces: 9.29

Max angle on Tri faces > 170: 0 (0%)

Average max angle on tri faces: 84.54, Worst max angle on tri faces: 134.52

Aspect ratio > 10: 0 (0%)

Average aspect ratio: 1.54, Worst aspect ratio: 6.19

Shape factor < 0.0001: 0 (0%)

Average shape factor: 0.735352, Worst shape factor: 0.045612

Analysis errors: 0 (0%), Analysis warnings: 1 (0.00122642%)

A.2 Sensitivity Analysis for Effect of Poisson's Ratio on Basilar Thumb Joint Model

Finite element models for the same subject were completed with only changes in the Poisson's ratio (Table A.2.1). Changes in contact area between a Poisson's ratio of 0.05 and 0.2 were under 5%. Changes in contact area between a Poisson's ratio of 0.2 and 0.3 were also under 5%. Small changes in magnitude for the other contact measures were observed. This indicates that the model is relatively insensitive to changes in Poisson's ratio below 0.3. A Poisson's ratio above 0.3 would not be appropriate for our models given the long-term loading during the MRI scan.

Table A.2.1. Contact Area (CA), Contact Force (CF), Average Pressure (AP), and Peak Pressure (PP) for Poisson's Ratios (PR) ranging from 0.05-0.45

PR	0.05	0.1	0.15	0.2	0.25	0.3	0.35	0.4	0.45
CA (mm^2)	15.256	15.331	15.459	15.650	16.014	16.35	16.831	17.692	18.789
CF (N)	1.312	1.343	1.391	1.465	1.574	1.739	2.000	2.461	3.473
AP (MPa)	0.077	0.079	0.081	0.085	0.09	0.097	0.111	0.131	0.178
PP (MPa)	0.242	0.247	0.255	0.266	0.282	0.307	0.346	0.406	0.544

A.3 Contact Pressure Maps from Micropipette Basilar Thumb Joint Models for all Four Subjects

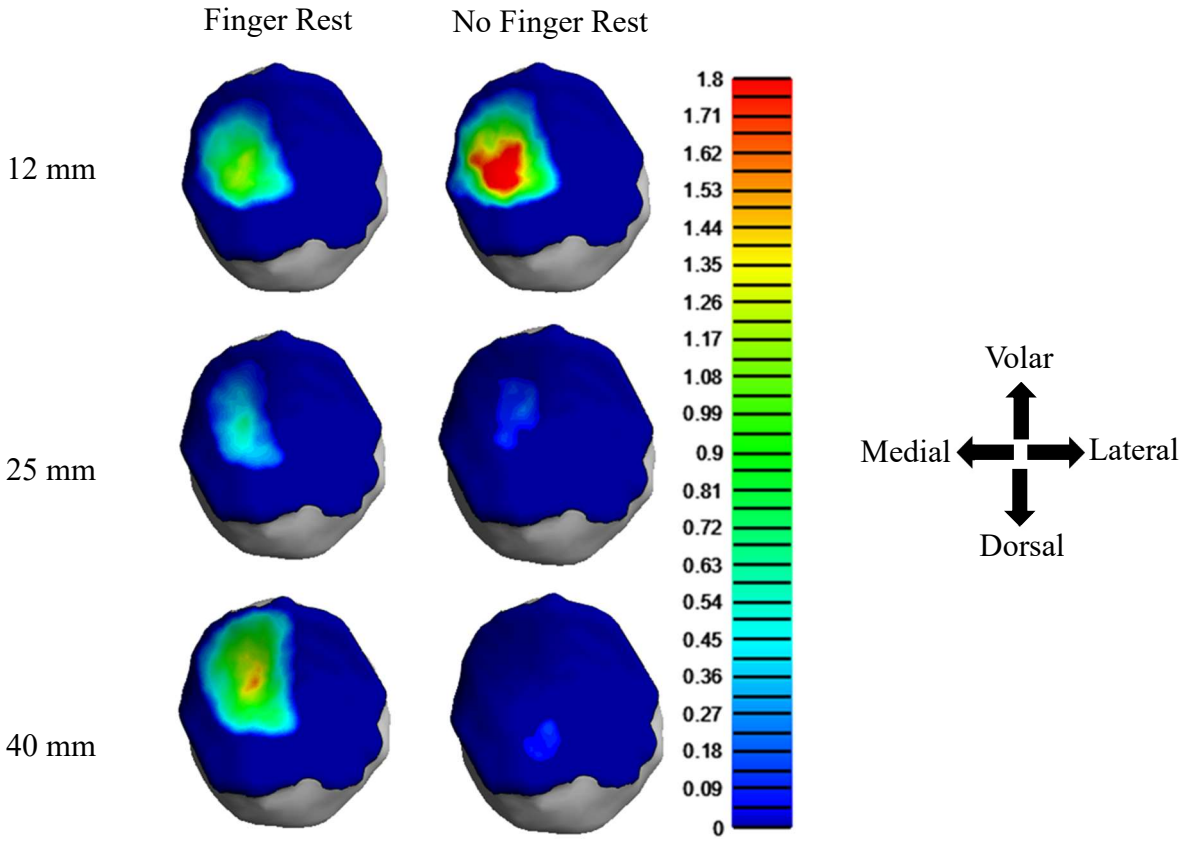

Figure A.3.1. Contact pressure plots for subject one(1). Contact pressure location was consistent across conditions except for the 40 mm handle without a finger rest. Contact pressure was the largest for the 12 mm diameter and decreased with increasing handle diameter except for the 40 mm handle with a finger rest.

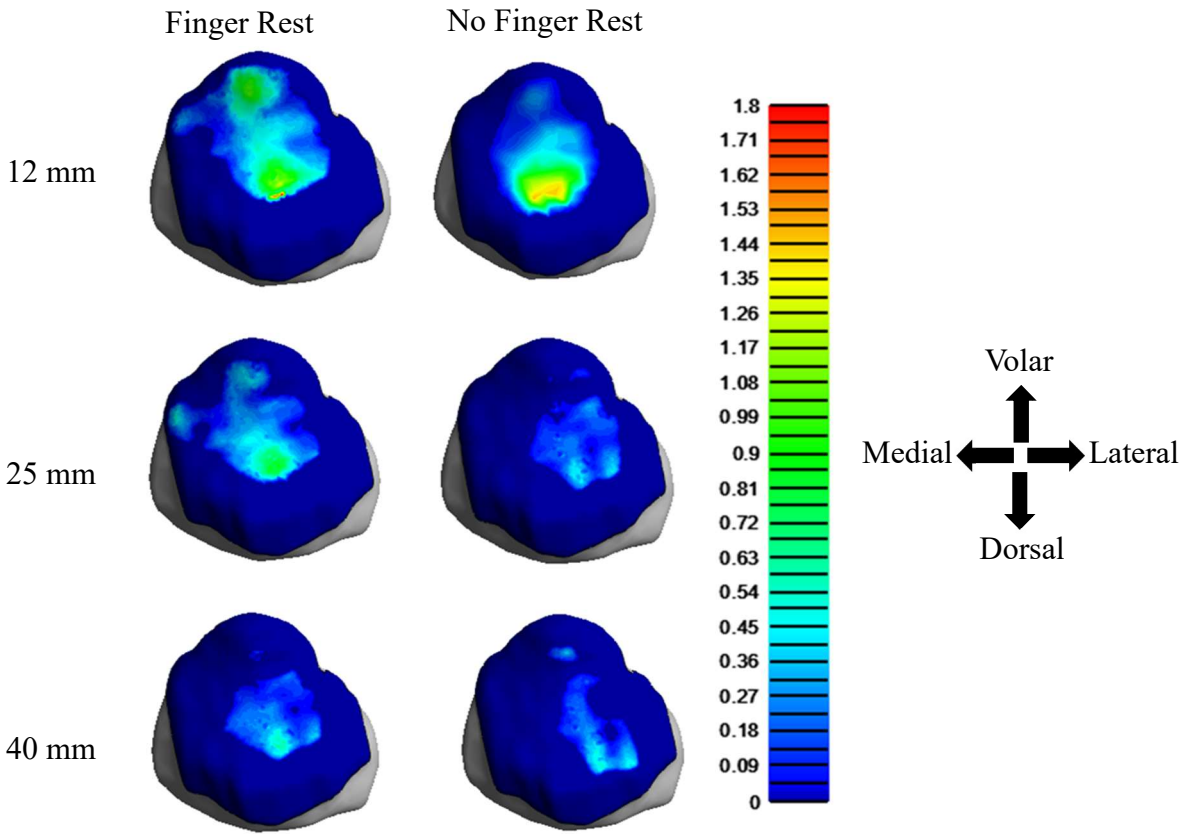

Figure A.3.2. Contact pressure plots for subject two(2). Contact pressure location was consistent across conditions. Contact pressure was the largest for the 12 mm diameter and decreased with increasing handle diameter.

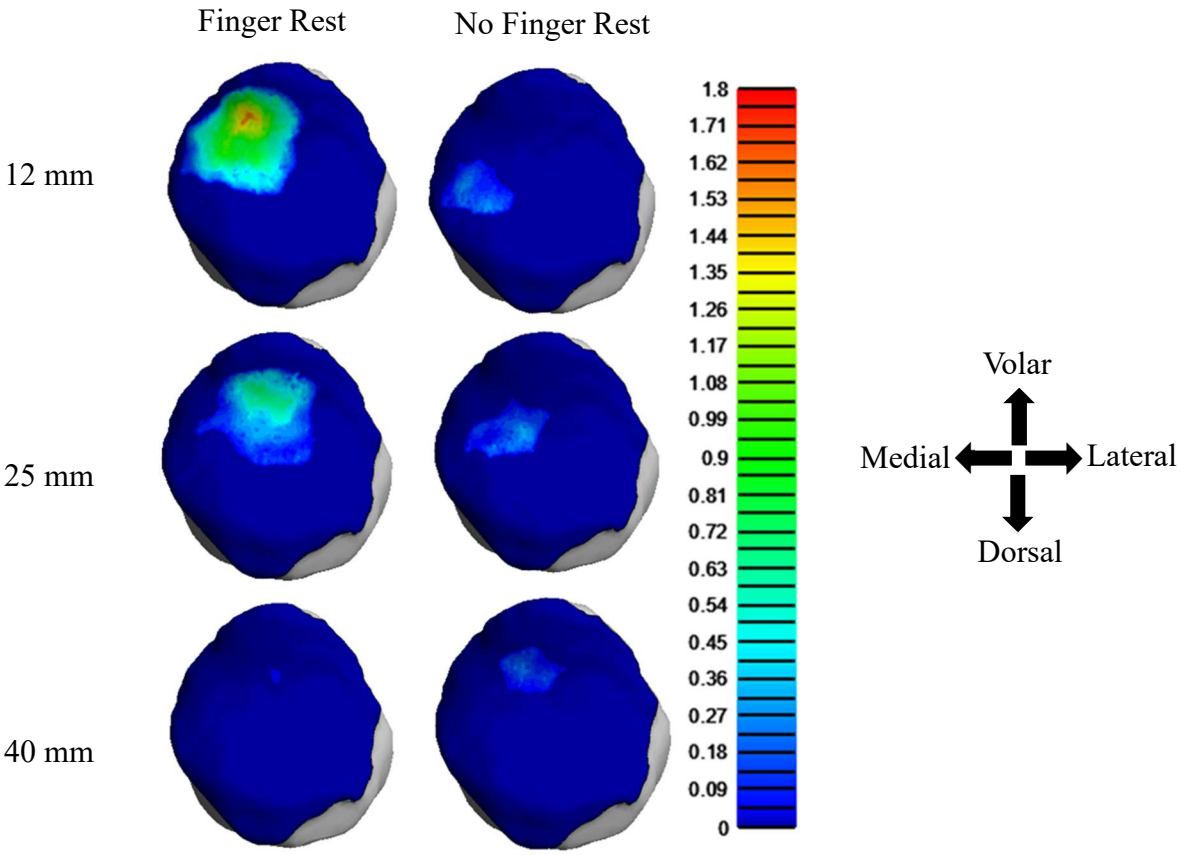

Figure A.3.3. Contact pressure plots for subject three(3). Contact pressure location was consistent across conditions. Contact pressure was the largest for the 12 mm diameter and decreased with increasing handle diameter.

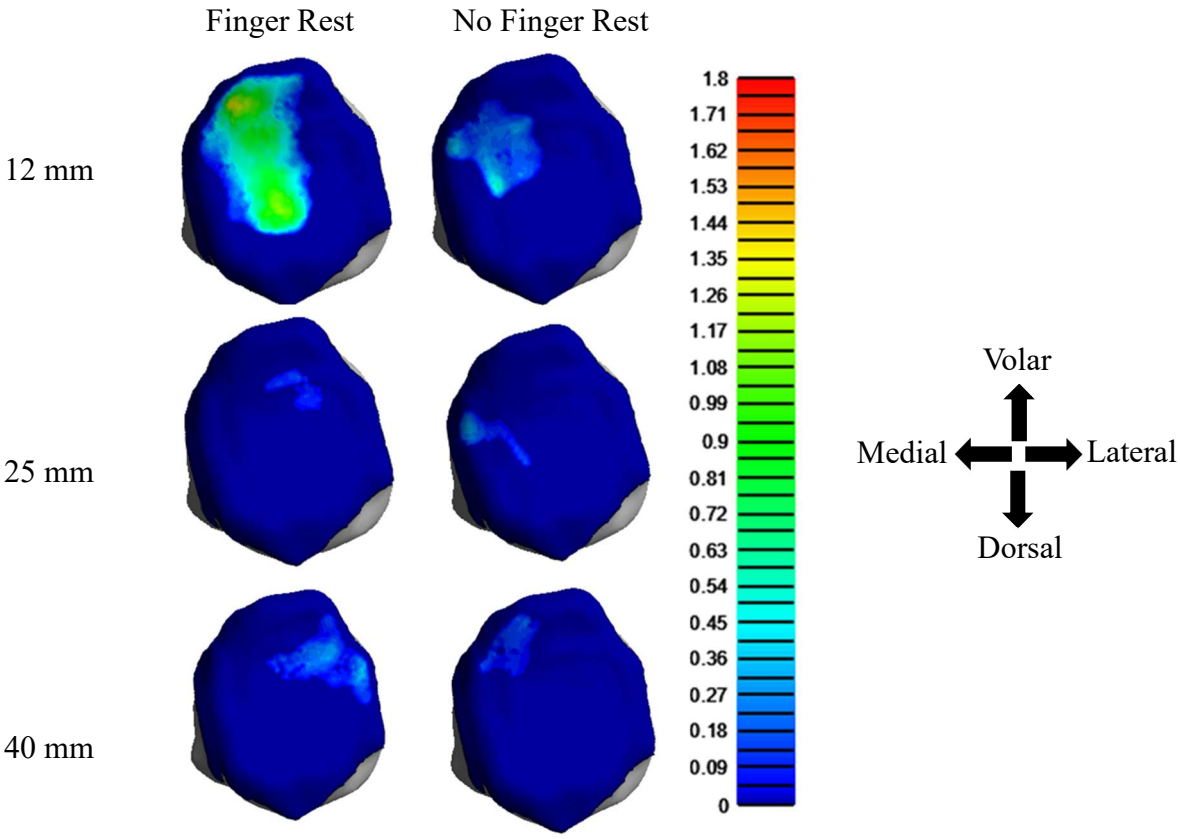

Figure A.3.4. Contact pressure plots for subject four(4). Contact pressure location was consistently volar across conditions. Contact pressure was the largest for the 12 mm diameter.

A.4 Visual Plots to Check Repeated Measures ANOVA Assumptions

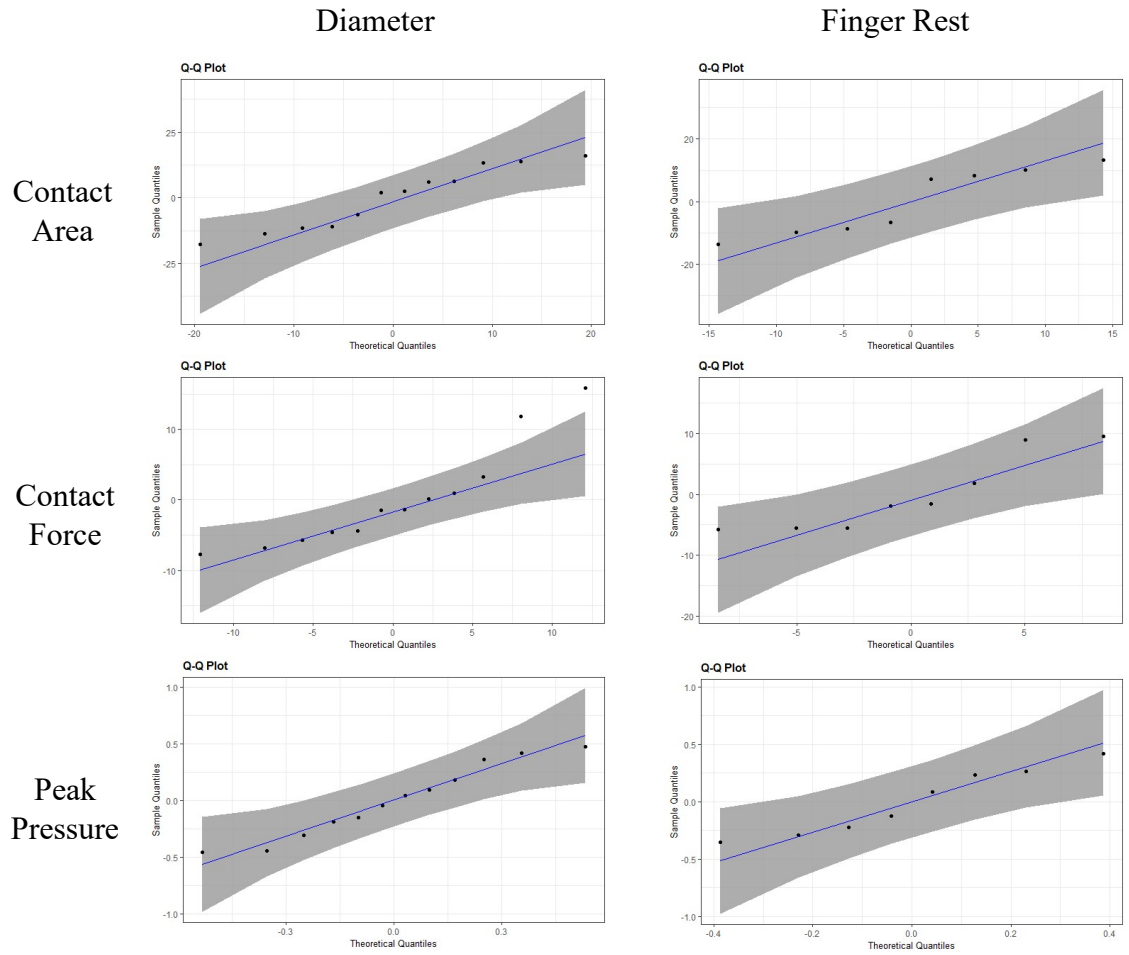

Figure A.4.1. Q-Q plots to assess normality for the one-way repeated measures ANOVA. Most of the plotted residuals are along the line of the theoretical quantiles of the normal distribution (blue line) and within the 95% confidence interval (shaded region).